

A *Suzaku* sample of unabsorbed narrow-line and broad-line Seyfert 1 galaxies: I. X-ray spectral properties

S. G. H. Waddell¹[★] and L. C. Gallo¹

¹*Department of Astronomy & Physics, Saint Mary's University, 923 Robie Street, Halifax, Nova Scotia, B3H 3C3, Canada*

Accepted XXX. Received YYY; in original form ZZZ

ABSTRACT

A sample of narrow-line (NLS1) and broad-line Seyfert 1 (BLS1) galaxies observed with *Suzaku* is presented. The final sample consists of 22 NLS1s and 47 BLS1s, for a total of 69 AGN that are all at low redshift ($z < 0.5$) and exhibit low host galaxy column densities ($< 10^{22} \text{ cm}^{-2}$). The average spectrum for each object is fit with a toy model to characterise important parameters, including the photon index, soft excess, Compton hump (or hard excess), narrow iron line strength, luminosity and X-ray Eddington ratio (L_x/L_{Edd}). We confirm previous findings that NLS1s have steeper power laws and higher X-ray Eddington ratios, but also find that NLS1 galaxies have stronger soft and hard excesses than their BLS1 counterparts. Studying the correlations between parameters shows that the soft and hard excesses are correlated for NLS1 galaxies, while no such correlation is observed for BLS1s. Performing a principal component analysis (PCA) on the measured X-ray parameters shows that while the X-ray Eddington ratio is the main source of variations within our sample (PC1), variations in the soft and hard excesses form the second principal component (PC2) and it is dominated by the NLS1s. The correlation between the soft and hard excess in NLS1 galaxies may suggest a common origin for the two components, such as a blurred reflection model. The presented *Suzaku* sample of Seyfert 1 galaxies is a useful tool for analysis of the X-ray properties of AGN, and for the study of the soft and hard excesses observed in AGN.

Key words: galaxies: active – galaxies: nuclei – X-rays: galaxies

1 INTRODUCTION

Active Galactic Nuclei (AGN) are accreting supermassive black holes at the centres of galaxies. These objects are responsible for some of the most energetic events in the Universe, and in many cases, can even outshine their host galaxies. By studying the X-ray emission from these objects, we are able to probe some of the most extreme processes occurring at the innermost regions of the AGN.

The X-ray spectra of Seyfert 1 galaxies (optical type-1), where we have a direct view of the central region, show key similarities. The primary component exhibits a power law shape across the entire X-ray band and is attributed to the Comptonisation of accretion disc photons in the hot corona surrounding the inner disc (e.g. Haardt & Maraschi 1991, 1993). Below 2 keV, many AGN exhibit a surplus of photons, called the soft excess, above the primary power law. The origin of the soft excess is highly disputed, and many possible physical interpretations exist to explain this feature, including a partial covering or obscuration scenario (e.g. Gierliński & Done 2004; Tanaka et al. 2004), blurred reflection originating in the inner accretion disc (e.g. Ballantyne et al. 2001; Ross & Fabian 2005), and soft Comptonisation of X-ray photons by a secondary, cooler

corona (e.g. Magdziarz et al. 1998; Done et al. 2012). These models have all been used successfully to explain the spectra of Seyfert 1 AGN.

At higher energies, a second excess, called the hard excess, peaking at ~ 20 keV is often detected. When hard X-ray photons produced in the corona are incident on optically thick material, they are scattered to lower energies through Compton down-scattering resulting in the so called Compton hump.

In the 4 – 7 keV band, AGN spectra show other important features, mainly those associated with iron. Interaction of the primary X-rays with iron in the surround medium can produce a strong X-ray fluorescent emission line at 6.4 keV if the material is neutral. This line may be narrow when coming from the distant torus (e.g. Nandra et al. 2007), or relativistically broadened due to the proximity to the supermassive black hole if it originates in the accretion disc (e.g. Fabian et al. 1989). Typically, we see a superimposition of these two lines, where both the torus and inner accretion disc are illuminated by the corona and thus a narrow core and extended line profile are seen simultaneously (e.g. Pounds et al. 1990; Nandra & Pounds 1994; Reeves et al. 2006).

Type-1 AGN are classified based on their optical spectra. NLS1s are those AGN with the full-width-half-maximum (FWHM) of the $H\beta$ lines less than 2000 km s^{-1} , while BLS1s have FWHM

[★] E-mail: swaddell@mpe.mpg.de

greater than 2000 km s^{-1} (Osterbrock & Pogge 1985; Goodrich 1989). NLS1 galaxies also show strong Fe II emission lines, and weak emission from forbidden [O III] lines.

The differences in the spectra and properties of BLS1 and NLS1 AGN beyond their optical properties is an important area of study. In general, it is observed that NLS1 AGN have lower mass black holes than their BLS1 counterparts. These smaller AGN have weaker gravitational fields, which may be partially responsible for the narrower optical lines produced in the broad line region of NLS1 galaxies. Additionally, it has been shown that NLS1 AGN are more rapidly accreting than their broad-line counterparts (Pounds et al. 1995; Grupe 2004; Grupe et al. 2010). NLS1s are often found to be accreting at a significant fraction of their Eddington limit. Together with the lower black hole mass, these pieces of information suggest that NLS1s may be a younger population of AGN (see for example, Grupe 1996; Mathur 2000). If this is indeed the case, the study of NLS1 galaxies and the comparison of their spectral properties to other Seyfert 1 AGN may lead to important clues on the growth and evolution of supermassive black holes throughout cosmic time.

In the X-ray regime, many NLS1 and BLS1 galaxies show large amplitude variability in their luminosities on very short timescales of hours (e.g. Nikołajuk et al. 2009; Gallo 2018). The variability in NLS1 galaxies is more extreme (e.g. Boller et al. 1996), and flux changes by factors of ~ 100 within days have been observed. The reason for this variability is not well understood, but may be correlated with the mass and/or accretion rates of the black holes (e.g. Ponti et al. 2012; Nikołajuk et al. 2009, and references therein). However, the very short timescales (hours) on which this variability is observed implies that X-rays originate from a very small and compact region, much smaller than the radius of the outer accretion disc or the BLR. The driving mechanism for this variability is therefore often associated with changes in the temperature, density and/or shape of the X-ray emitting corona (e.g. Wilkins et al. 2015; Gallo et al. 2019; Alston et al. 2019).

Boller et al. (1996) examined the soft X-ray spectra of a sample of NLS1 AGN observed with *ROSAT*. They found that NLS1 galaxies have very steep spectral slopes of $\Gamma \approx 3.5$ at low energies (0.1 – 2.4 keV), where Γ is the power law photon index. This is much steeper than typical BLS1 galaxies, which have indices of $\Gamma \approx 2.3$ in this energy range (Walter & Fink 1993). These results are confirmed by Leighly (1999), who perform a similar analysis on a sample of NLS1 AGN observed with *ASCA*, and other subsequent works. Additionally, NLS1 galaxies have been shown to show stronger soft excesses, or increased excess emission below $\sim 2 \text{ keV}$ using a variety of toy models (e.g. Vaughan et al. 1999; Grupe et al. 2010; Gliozzi & Williams 2020; Ojha et al. 2020), and some NLS1 galaxies also show extreme soft excesses (e.g. Gallo et al. 2004; Middleton et al. 2007). These properties suggest that the soft excesses of NLS1 AGN may differ from those of BLS1 AGN.

The X-ray spectral slopes of NLS1 galaxies in the 2 – 10 keV energy range have also been shown to be steeper than those of BLS1 galaxies (e.g. Brandt et al. 1997; Grupe 2004). This range is expected to be dominated by emission from the corona, which takes the form of a power law. Like the rapid variability, this may point to differences in the temperature of the corona (Gallo 2006, 2018), where in particular, cooler coronae produce steeper X-ray spectral slopes (Pounds et al. 1995). Clearly, NLS1 galaxies occupy an extreme parameter space in many respects and are worthy of further analysis.

Many previous works have taken advantage of the broad-band

observing capabilities of *Suzaku* for the analyses of samples of AGN. These range significantly in scope, from Fe $K\alpha$ line profile studies (e.g. Fukazawa et al. 2011, 2016; Mantovani et al. 2016) and physical spectral modelling (e.g. Noda et al. 2013; Walton et al. 2013a; Iso et al. 2016) to spectral variability studies (e.g. Miyazawa et al. 2009).

In this work, we present a sample of NLS1 and BLS1 AGN observed with the *Suzaku* satellite in order to characterise their X-ray spectral properties, and investigate differences between the two classes. This work will expand upon previous samples by including a larger number of optical type-1 AGN, and studying the properties of NLS1 and BLS1 galaxies. The goal is to examine a range of parameters from the soft to hard band to search for similarities and differences between the two classes. In Section 2, we describe the sample selection and present literature parameters for each AGN. In Section 3, we describe the data analysis. Section 4 describes the spectral model used for analysis and discusses parameter distributions. In Section 5, we present correlations between parameters and compare the two samples. A discussion of results is given in Section 6, and conclusions are presented in Section 7.

2 SAMPLE SELECTION

The X-ray observatory used for this work is the *Suzaku* satellite (Mitsuda et al. 2007), operational between 2005 and 2015. The observatory collected data using two main detectors; the four X-ray Imaging Spectrometers (XIS) and the Hard X-ray Detector (HXD). The HXD instrument includes the PIN and GSO detectors intended for the capture of high energy X-rays. By combining data from the XIS and PIN detectors, *Suzaku* is sensitive between ~ 0.5 –100 keV, allowing for the simultaneous observation of the X-ray soft excess, power law emission from the corona, Fe $K\alpha$ emission and Compton hump. The simultaneous detection of all these components allows for detailed, broad-band X-ray spectral characterisation.

The sample is assembled to include objects that exhibit relatively small levels of absorption so that the low-energy emission (i.e. the soft excess) can be constrained. All *Suzaku* observations used in this work are publicly available on the *Suzaku* DARTS¹ website. These observations are divided into several sub-categories based on object class. AGN are typically classified as extra-galactic compact sources, and we thus begin our search for Seyfert 1 galaxies in this sub-section. In total, 518 observations of approximately 350 sources were made over the mission lifetime. Of these, 225 were found to be Seyfert galaxies, with 106 being type-1 AGN.

We first selected all Seyfert 1, 1.2, and 1.5 galaxies, as these objects are expected to show little X-ray absorption due to obscuration by the torus. We include only those galaxies with intrinsic (host-galaxy) column densities of less than 10^{22} cm^{-2} , allowing for some constraint to be placed on the soft excess component. Objects with redshifts $z > 0.5$ are also excluded to ensure that the intrinsic spectrum down to at least $\sim 1 \text{ keV}$ could be measured.

The remaining 72 objects were then divided into sub-samples of NLS1 and BLS1 galaxies based on classifications found in literature. All the NLS1s have $\text{FWHM}(H\beta) < 2000 \text{ km s}^{-1}$, relatively strong Fe II and weak [O III] according to previous works. One source, MCG+04-22-042, has several different measurements for the $\text{FWHM}(H\beta)$, with the smallest width recorded as $1946 \pm$

¹ <https://darts.isas.jaxa.jp/astro/suzaku/>

(1) Object	(2) Redshift	(3) N _H [$\times 10^{22}$ cm ⁻²]	(4) FWHM (H β) [km s ⁻¹]	(5) M _{BH} [$\times 10^7$ M _{Sun}]
NLS1				
1H0323+342	0.061	0.127	1520 ⁽¹⁾	2.00 ⁽²⁾
1H0707-495	0.04057	0.0431	1000 ⁽³⁾	0.204 ⁽⁴⁾
Ark 564	0.02468	0.0534	750 ⁽³⁾	0.186 ⁽⁵⁾
IRAS 05262+4432	0.03217	0.321	700 ⁽³⁾	2.06 ⁽⁶⁾
IRAS 13224-3809	0.0658	0.0476	650 ⁽³⁾	0.631 ⁽⁷⁾
MCG-6-30-15	0.00775	0.0392	1700 ⁽⁴⁾	0.200 ⁽⁵⁾
Mrk 1040	0.01665	0.0673	1830 ⁽⁶⁾	4.37 ⁽⁷⁾
Mrk 110	0.03529	0.013	1760 ⁽⁸⁾	1.96 ⁽⁹⁾
Mrk 335	0.02578	0.0356	1710 ⁽⁸⁾	1.70 ⁽⁹⁾
Mrk 359	0.01739	0.0426	900 ⁽⁶⁾	0.170 ⁽⁶⁾
Mrk 478	0.07906	0.0105	1630 ⁽⁸⁾	1.99 ⁽¹⁰⁾
Mrk 766	0.01293	0.0178	1100 ⁽⁸⁾	0.664 ⁽⁹⁾
NGC 4051	0.00234	0.0115	1170 ⁽⁸⁾	0.135 ⁽⁹⁾
PG 1211+143	0.0809	0.0274	1900 ⁽⁸⁾	4.07 ⁽⁵⁾
PG 1404+226	0.098	0.0222	880 ⁽³⁾	0.450 ⁽¹¹⁾
PKS 0558-504	0.1372	0.036	1250 ⁽¹²⁾	4.50 ⁽¹²⁾
RE J1034+396	0.04244	0.04244	1500 ⁽⁴⁾	0.245 ⁽¹³⁾
RX J0134.2-4258	0.237	0.0167	900 ⁽⁸⁾	2.00 ⁽¹⁴⁾
RX J1633.3+4718	0.1158	0.0174	900 ⁽¹⁵⁾	0.300 ⁽¹⁵⁾
SWIFT J2127.4+5654	0.0144	0.765	2000 ⁽¹⁶⁾	1.51 ⁽¹⁶⁾
TON S180	0.06198	0.0136	970 ⁽⁸⁾	0.710 ⁽⁹⁾
WKK 4438	0.016	0.291	1700 ⁽¹⁶⁾	0.200 ⁽⁶⁾
BLS1				
1H0419-577	0.104	0.0116	2580 ⁽⁸⁾	13.0 ⁽⁸⁾
3C 111	0.0485	0.285	4800 ⁽¹⁷⁾	360 ⁽¹⁷⁾
3C 120	0.03301	0.194	3711 ⁽¹⁸⁾	5.50 ⁽⁹⁾
3C 382	0.05787	0.0619	...	61.7 ⁽¹⁹⁾
3C 390.3	0.0561	0.0441	10000 ⁽⁴⁾	43.5 ⁽⁹⁾
3C 78	0.02865	0.104	...	39.8 ⁽²⁰⁾
4C+74.26	0.104	0.114	11000 ⁽²¹⁾	398 ⁽²²⁾
Ark 120	0.03271	0.0998	5800 ⁽⁴⁾	11.7 ⁽⁹⁾
B3 0309+411	0.136	0.101
CBS 126	0.0791	0.0131	2980 ⁽⁸⁾	7.09 ⁽⁸⁾
ESO 511-G030	0.02239	0.0434	3335 ⁽²³⁾	6.92 ⁽¹⁹⁾
ESO 548-G081	0.01448	0.0237	...	5.50 ⁽¹⁹⁾
Fairall 9	0.04702	0.0286	5780 ⁽⁴⁾	19.9 ⁽⁹⁾
IGR J16185-5928	0.03463	0.207	2918 ⁽²³⁾	2.80 ⁽²⁴⁾
IGR J19378-0617	0.01025	0.191	2700 ⁽²⁴⁾	...
III Zw 2	0.0898	0.0592	5295 ⁽²³⁾	11.7 ⁽⁹⁾
KAZ 102	0.136	0.0475	...	10.0 ⁽²⁵⁾
LEDA 168563	0.029	0.437	7400 ⁽²⁶⁾	11.0 ⁽²⁶⁾
MCG-02-14-009	0.02845	0.1	...	1.35 ⁽⁵⁾
MCG-02-58-22	0.04686	0.0334	6360 ⁽⁴⁾	30.0 ⁽²⁷⁾
MCG+04-22-042*	0.03235	0.035	2600 ⁽²³⁾	31.6 ⁽²²⁾
MCG+08-11-11	0.02048	0.297	3630 ⁽⁴⁾	12.0 ⁽²⁸⁾
MR 2251-178	0.06398	0.0264	4617 ⁽²³⁾	19.0 ⁽²⁹⁾
Mrk 1018	0.04244	0.0267	5858 ⁽³⁰⁾	6.92 ⁽³¹⁾
Mrk 1148	0.064	0.0501
Mrk 1320	0.103	0.024
Mrk 205	0.07085	0.029	4560 ⁽²³⁾	20.9 ⁽⁵⁾
Mrk 279	0.03045	0.0159	5360 ⁽⁴⁾	2.72 ⁽⁹⁾
Mrk 352	0.01486	0.0531	4214 ⁽²³⁾	0.85 ⁽³²⁾
Mrk 509	0.0344	0.0393	2270 ⁽⁴⁾	11.2 ⁽⁹⁾
Mrk 530	0.02952	0.0442	...	11.5 ⁽³³⁾

(1) Object	(2) Redshift	(3) N _H [$\times 10^{22}$ cm ⁻²]	(4) FWHM (H β) [km s ⁻¹]	(5) M _{BH} [$\times 10^7$ M _{Sun}]
Mrk 79	0.02219	0.0543	4000 ⁽²³⁾	4.09 ⁽⁹⁾
Mrk 841	0.03642	0.0246	5470 ⁽⁴⁾	7.59 ⁽³⁴⁾
NGC 4593	0.009	0.0167	4910 ⁽⁸⁾	0.950 ⁽⁸⁾
NGC 6814	0.00521	0.148	...	1.09 ⁽⁹⁾
NGC 7213	0.00584	0.0111	13000 ⁽³⁵⁾	10.00 ⁽³⁵⁾
NGC 7469	0.01632	0.0539	3388 ⁽⁴⁾	0.904 ⁽⁹⁾
NGC 985	0.04314	0.0346
PG 1322+659	0.168	0.017	...	19.5 ⁽³⁶⁾
PG 1626+554	0.133	0.0108	...	53.7 ⁽³⁷⁾
RBS 1124	0.208	0.0156	...	18.0 ⁽³⁸⁾
SBS 1301+540	0.0299	0.0173	7174 ⁽²³⁾	3.16 ⁽²²⁾
SWIFT J0501.9-3239	0.01244	0.0184
SWIFT J0904.3+5538	0.03714	0.0232	3022 ⁽²³⁾	...
SWIFT J1310.9-5553	0.104	0.208
UGC 6728	0.00652	0.0446	2308 ⁽³⁰⁾	0.513 ⁽⁹⁾
ZW 229-15	0.02788	0.0534	3360 ⁽³⁹⁾	0.818 ⁽⁹⁾

Table 1: AGN parameters for all NLS1s and BLS1s in the *Suzaku* sample. Column (1) gives the object name, and columns (2) and (3) show the redshift and Galactic column density, obtained from NED and [Willingale et al. \(2013\)](#), respectively. Columns (4) and (5) show the FWHM and black hole mass for each source. One source, MCG+04-22-042, is included in the BLS1 sample but has been alternatively classified as an NLS1 and is marked with an asterisk. Masses and FWHM values are taken from: (1) [Paliya et al. \(2014\)](#); (2) [Landt et al. \(2017\)](#); (3) [Vaughan et al. \(1999\)](#); (4) [Bian & Zhao \(2003\)](#); (5) [Ponti et al. \(2012\)](#). (6) [Wang & Lu \(2001\)](#); (7) [González-Martín & Vaughan \(2012\)](#); (8) [Grupe et al. \(2010\)](#); (9) [Bentz & Katz \(2015\)](#); (10) [Porquet et al. \(2004\)](#); (11) [Mallick & Dewangan \(2018\)](#); (12) [Gliozzi et al. \(2007\)](#); (13) [Czerny et al. \(2016\)](#); (14) [Grupe et al. \(2000\)](#); (15) [Yuan et al. \(2010\)](#); (16) [Malizia et al. \(2008\)](#); (17) [Ballo et al. \(2011\)](#); (18) [Du et al. \(2018\)](#); (19) [Vasudevan & Fabian \(2009\)](#); (20) [Woo & Urry \(2002\)](#); (21) [Ballantyne \(2005\)](#); (22) [Soldi et al. \(2014\)](#); (23) [Koss et al. \(2017\)](#); (24) [Malizia et al. \(2008\)](#); (25) [Miyaji et al. \(2003\)](#); (26) [Liebmann et al. \(2018\)](#); (27) [Rivers et al. \(2011\)](#); (28) [Tortosa \(2017\)](#); (29) [Wang et al. \(2009\)](#); (30) [Winter et al. \(2010\)](#); (31) [Noda & Done \(2018\)](#); (32) [Vasudevan et al. \(2009\)](#); (33) [Woo et al. \(2012\)](#); (34) [Vestergaard \(2002\)](#); (35) [Nelson & Whittle \(1995\)](#); (36) [You et al. \(2016\)](#); (37); [Vasudevan & Fabian \(2007\)](#); (38) [Miniutti et al. \(2010\)](#); (39) [Barth et al. \(2011\)](#).

170 km s⁻¹ (La Mura et al. 2011). This borderline object is included in the BLS1 sample and marked with an asterisk in Table 1. It appears comparable to other BLS1s in our analysis.

Two objects, Mrk 1239 (typically classified as an NLS1) and ESO 323-G077 (BLS1), were rejected from the sample as they exhibited atypical spectra (see Grupe et al. 2004 and Buhariwalla et al. 2020 for Mrk 1239, and Miniutti et al. 2014 for ESO 323-G077). Both AGN show significant optical polarization and ESO 323-G077 has been described as a borderline Seyfert 1/2 (e.g. Schmid et al. 2003). Mrk 590, typically classified as BLS1, was also removed. This source has been shown to change look (i.e., show dramatic optical emission line variability), and although typically classified as a Seyfert 1, did not show a typical type-1 optical spectrum during the *Suzaku* observation (Mathur et al. 2018). Additionally, only two out of the six observations of the BLS1 galaxy 3C 120 are included here due to calibration uncertainties during the first four observations, which were taken during the calibration phase. The final sample consists of 22 narrow-line Seyfert 1 AGN, and 47 broad-line Seyfert 1 AGN, for a total of 69 AGN suitable for analysis.

To characterise our sample, we first perform a literature search to determine the black hole mass and H β FWHM of each object. Redshifts for each object are taken from NED², and column densities viewed through the Galaxy are taken from Willingale et al. (2013). The results, where available, are presented in Table 1. The sample covers a redshift range of $z = 0.00234$ to $z = 0.237$, with most AGN having $z < 0.1$. NLS1 galaxies appear to have lower black hole masses on average than their BLS1 counterparts, in agreement with previous observations (e.g. Pounds et al. 1995; Wang et al. 1996; Grupe 2004; Grupe et al. 2010).

3 DATA REDUCTION

3.1 *Suzaku* XIS

The *Suzaku* XIS detectors feature four CCD cameras; XIS0, XIS1, XIS2 and XIS3. In late 2006, the XIS2 detector was struck by a small meteorite and became unsuitable for use in scientific analysis, so observations taken after November 2006 have data from only three XIS detectors. The XIS1 detector differs from the others in that it is back-illuminated (BI). The detector response is significantly different from the other three front-illuminated (FI) CCDs, and can not be co-added with the other detectors. XIS1 has very high background at high energies (above ~ 7 keV), which complicates analysis of the Fe K α line profile. For the remainder of this work, we therefore focus only on the FI detectors XIS0 and XIS3 (and XIS2 when available).

Cleaned event files from the FI CCDs were used for the extraction of data products in XSELECT v2.4G. For each instrument, source photons were extracted using a 240'' region centred around the source, while background photons were extracted from a 180'' off-source region. Calibration zones located in the corners of the CCDs were avoided in the background extraction. Response matrices for each detector were generated using the tasks XISRMFGEN and XISSIMARFGEN. The data and responses from each of the FI detectors were then merged to improve signal-to-noise.

In this work we are comparing overall average properties of the sample. The data from AGN observed at multiple epochs are merged to form one single spectrum for each unique source.

Source and background spectra, as well as responses are merged for each object, with spectra and responses weighted based on exposure time. The merged spectrum for each object is then used in spectral modelling for the remainder of this work. For each merged spectrum, we model the 0.6 – 10 keV energy band, excluding the calibration uncertainty regions between 1.72 – 1.88 keV and 2.19 – 2.37 keV (Nowak et al. 2011). Observations are summarized in Table 2.

3.2 *Suzaku* HXD

Data from the *Suzaku* HXD-PIN detector are also used in the analysis. In general, the 15 – 40 keV energy band is modelled, but for some objects, this band is smaller to improve the detection signal. Data are processed using the tool HXDPIXBPI. Both the non-X-ray background (NXB) and the cosmic X-ray background (CXB) are considered to determine the detection threshold for each observation, where a detection of 5 per cent of background is considered significant (Fukazawa et al. 2009). As with the XIS, data from individual observations of each source are merged to create one averaged spectrum for each source. A cross calibration factor between the PIN and the XIS of 1.16 or 1.18 is applied, depending on whether the observation was taken in XIS or HXD nominal pointing mode, respectively. The exception for this is NGC 6814, where a much lower calibration constant of 0.5 is required (Walton et al. 2013b). We also neglect the PIN data for Zw 229-15, as these data were shown to diverge significantly from all models and other high energy data sets, possibly due to low data quality or calibration uncertainties (Tripathi et al. 2019).

4 SPECTRAL MODELLING

4.1 Modelling procedure

All spectral fits are performed using XSPEC v12.9.0N (Arnaud 1996) from HEASOFT v6.26. Abundances are taken from Wilms et al. 2000, and values for the Galactic column density for each source are taken from Willingale et al. (2013). Spectra from the *Suzaku* XIS detectors have been grouped using optimal binning (Kaastra & Bleeker 2016), using the FTGROUPPHA tool, while data from the PIN have been grouped to a minimum of 20 counts per bin. Model fitting was done using C-statistic (Cash 1979), to account for the fact that the data do not follow a Gaussian distribution, but rather a Poisson distribution. All errors are quoted at the 90 per cent confidence level. For ease of comparison between objects, luminosities free of Galactic and host-galaxy absorption, rather than fluxes or model normalisations, are presented. These luminosities are calculated using the LUMIN command in XSPEC. We adopt a value for the Hubble constant of $H_0 = 70$ km s⁻¹ Mpc⁻¹, and $\Lambda_0 = 0.73$.

To maximize the spectral information from each observation, we model the XIS background spectrum obtained from the off-source regions rather than simply subtracting it. This is required when using C-statistics, and allows for improved analysis of dim sources which are background dominated at high energies, such as 1H0707-495 (Fig. 1). This source becomes dominated by emission from the background above ~ 6 keV (see the background subtracted spectrum in blue), but by modelling the background, we can consider up to 10 keV.

² <https://ned.ipac.caltech.edu/>

(1) Object	(2) Obs ID	(3) Date YYYY-MM-DD	(4) Detector	(5) Exposure (s) (all XIS)	(6) SC cts (all XIS)	(7) BG cts (all XIS)	(8) PIN cts	(9) PIN %
NLS1								
1H0323+342	704034010	2009-07-26	XIS 0+3	371000	232762	5491	40370	9.0
	707015010	2013-03-01	XIS 0+3					
1H0707-495	700008010	2005-12-03	XIS 0+2+3	292900	23750	3938	16720	2.9*
Ark 564	702117010	2007-06-26	XIS 0+3	306400	886516	8138	27061	8.4
	710018010	2015-05-25	XIS 0+3					
IRAS 05262+4432	703019010	2008-09-12	XIS 0+3	164200	16817	1907	12503	2.1*
IRAS 13224-3809	701003010	2007-01-26	XIS 0+3	395900	49337	5192	-	-
MCG-6-30-15	700007010	2006-01-09	XIS 0+2+3	1015000	2797730	23791	115952	23.3
	700007020	2006-01-23	XIS 0+2+3					
	700007030	2006-01-27	XIS 0+2+3					
Mrk 1040	707046010	2013-08-11	XIS 0+3	274900	533369	8471	36897	31.1
Mrk 110	702124010	2007-11-02	XIS 0+3	181800	229892	3684	27197	15.8
Mrk 335	701031010	2006-06-21	XIS 0+2+3	1052000	702650	16100	43096	9.2
	708016020	2013-06-14	XIS 0+3					
	708016010	2013-06-11	XIS 0+3					
Mrk 359	701082010	2007-02-06	XIS 0+3	215000	79777	2776	19905	4.1*
Mrk 478	706041010	2011-07-14	XIS 0+3	170600	43759	2070	13877	3.1*
Mrk 766	701035010	2006-11-16	XIS 0+3	315100	277229	3996	45721	9.0
	701035020	2007-11-17	XIS 0+3					
NGC 4051	703023010	2008-11-06	XIS 0+3	1065000	1526650	6667	129761	15.3
	700004010	2005-11-10	XIS 0+2+3					
	703023020	2008-11-13	XIS 0+3					
PG 1211+143	700009010	2005-11-24	XIS 0+2+3	289200	86466	4345	17679	4.0*
PG 1404+226	708045010	2013-07-13	XIS 0+3	365400	12833	3818	24168	7.7
	707026010	2012-12-23	XIS 0+3					
PKS 0558-504	701011030	2007-01-19	XIS 0+3	200100	310836	2806	16297	8.2
	701011010	2007-01-17	XIS 0+3					
	701011040	2007-01-20	XIS 0+3					
	701011050	2007-01-21	XIS 0+3					
	701011020	2007-01-18	XIS 0+3					
RE J1034+396	707039010	2012-11-14	XIS 0+3	199800	34194	2098	14164	5.5
RX J0134.2-4258	707014010	2012-12-29	XIS 0+3	162900	34665	1627	1519	5.8
RX J1633.3+4718	706027040	2012-02-05	XIS 0+3	334200	35951	4043	21475	2.8*
	706027030	2012-01-13	XIS 0+3					
	706027010	2011-07-01	XIS 0+3					
	706027020	2011-07-08	XIS 0+3					
SWIFT J2127.4+5654	702122010	2007-12-09	XIS 3	91730	131319	2227	30599	20.6
TON S180	701021010	2006-12-09	XIS 0+3	241400	176949	3602	23364	4.8*
WKK 4438	706011010	2012-01-22	XIS 0+3	140600	91783	1446	13314	6.2
BLS1								
1H0419-577	702041010	2007-07-25	XIS 0+3	658000	770926	13936	48285	15.5
	704064010	2010-01-16	XIS 0+3					
3C 111	703034010	2008-08-22	XIS 0+3	725700	1153400	15114	27277	37.4
	705040010	2010-09-02	XIS 0+3					
	705040020	2010-09-09	XIS 0+3					
	705040030	2010-09-14	XIS 0+3					
3C 120	706042010	2012-02-09	XIS 0+3	602200	1665920	16153	89641	36.0
	706042020	2012-02-14	XIS 0+3					
3C 382	702125010	2007-04-27	XIS 0+3	261200	722194	5800	43401	24.7
3C 390.3	708034010	2013-05-24	XIS 0+3	200700	481139	3355	32140	32.1
3C 78	706013010	2011-08-20	XIS 0+3	194000	23330	2318	-	-
4C+74.26	702057010	2007-10-28	XIS 0+3	386000	562383	7614	32440	22.2
	706028010	2011-11-23	XIS 0+3					
Ark 120	702014010	2007-04-01	XIS 0+3	201700	410487	6401	32393	21.2
B3 0309+411	706036010	2012-02-19	XIS 0+3	209200	55068	3994	16910	2.4*
CBS 126	705042010	2010-10-18	XIS 0+3	203100	70422	2704	22703	4.2*
ESO 511-G030	707023020	2012-07-22	XIS 0+3	551900	725334	11944	13447	20.4
	707023030	2012-08-17	XIS 0+3					

(1) Object	(2) Obs ID	(3) Date YYYY-MM-DD	(4) Detector	(5) Exposure (s) (all XIS)	(6) SC cts (all XIS)	(7) BG cts (all XIS)	(8) PIN cts	(9) PIN %
ESO 548-G081	704026010	2009-08-03	XIS 0+3	78830	58808	1495	10054	13.8
Fairall 9	705063010	2010-05-19	XIS 0+3	794200	1350110	13064	103887	20.4
	702043010	2007-06-07	XIS 0+3					
IGR J16185-5928	702123010	2008-02-09	XIS 0+3	153200	73459	4219	22482	9.7
IGR J19378-0617	705055010	2010-10-16	XIS 0+3	155600	274166	4215	19433	11.0
III Zw 2	706031010	2011-06-14	XIS 0+3	162900	85023	2827	21272	10.4
KAZ 102	701012010	2006-06-09	XIS 0+3	82920	10915	1022	3298	3.1*
LEDA 168563	708017010	2013-09-01	XIS 0+3	200100	149668	3884	22645	19.2
MCG-02-14-009	703060010	2008-08-28	XIS 0+3	284300	73480	3786	24412	6.0
MCG-02-58-22	704032010	2009-12-02	XIS 0+3	278000	1009640	5994	39753	38.0
MCG+04-22-042	704028010	2009-11-22	XIS 0+3	81980	74668	1439	10480	12.3
MCG+08-11-11	702112010	2009-09-17	XIS 0+3	197500	572367	6899	39533	39.6
MR 2251-178	704055010	2009-05-07	XIS 0+3	273900	623692	4969	37765	26.7
Mrk 1018	704044010	2009-07-03	XIS 0+3	87820	55075	1551	10700	13.4
Mrk 1148	708033010	2013-12-30	XIS 0+3	56650	64418	835	5676	17.9
Mrk 1320	704006010	2009-06-28	XIS 0+3	41560	3448	530	-	-
Mrk 205	705062010	2010-05-22	XIS 0+3	201900	114219	4128	27039	14.1
Mrk 279	704031010	2009-05-14	XIS 0+3	320700	92008	3426	40011	9.2
Mrk 352	704025010	2010-01-06	XIS 0+3	91370	61034	1893	6303	8.0
Mrk 509	705025010	2010-11-21	XIS 0+3	471000	1689290	11724	70667	31.9
	701093040	2006-11-27	XIS 0+3					
	701093020	2006-10-14	XIS 0+2+3					
	701093010	2006-04-25	XIS 0+2+3					
	701093030	2006-11-15	XIS 0+3					
Mrk 530	707003010	2012-06-02	XIS 0+3	202500	313042	2667	25044	17.3
Mrk 79	702044010	2007-04-03	XIS 0+3	167400	131341	1941	25288	9.6
Mrk 841	701084010	2007-01-22	XIS 0+3	914700	686420	20200	119074	11.3
	701084020	2007-07-23	XIS 0+3					
	706029010	2012-01-05	XIS 0+3					
	706029020	2012-01-18	XIS 0+3					
NGC 4593	702040010	2007-12-15	XIS 0+3	971600	965252	15277	47703	16.0
	709014050	2014-12-30	XIS 0+3					
	709014040	2014-12-26	XIS 0+3					
	709014020	2014-06-22	XIS 0+3					
	709014030	2014-12-15	XIS 0+3					
	709014010	2014-06-16	XIS 0+3					
NGC 6814	706032010	2011-11-02	XIS 0+3	84260	36352	1046	10096	4.8*
NGC 7213	701029010	2006-10-22	XIS 0+2+3	272200	428912	4137	32255	16.2
NGC 7469	703028010	2008-06-24	XIS 0+3	224200	254110	4818	29828	19.3
NGC 985	704042010	2009-07-15	XIS 0+3	64000	47761	1263	7607	13.9
PG 1322+659	706018010	2011-11-27	XIS 0+3	163400	11544	1641	-	-
PG 1626+554	706017010	2011-11-11	XIS 0+3	121700	38611	1788	-	-
RBS 1124	702114010	2007-04-14	XIS 0+3	172500	48581	1816	27027	7.5
SBS 1301+540	709018010	2014-11-30	XIS 0+3	189500	47297	2000	13525	6.9
SWIFT J0501.9-3239	703014010	2008-04-11	XIS 0+3	82600	176307	2556	13042	24.3
SWIFT J0904.3+5538	704027010	2009-04-28	XIS 0+3	83890	11307	989	6885	5.7
SWIFT J1310.9-5553	706009010	2011-07-19	XIS 0+3	165600	41357	1993	17854	6.5
UGC 6728	704029010	2009-06-06	XIS 0+3	98010	80844	1710	12202	13.5
ZW 229-15	706035010	2011-06-03	XIS 0+3	337400	91424	5253	-	-

Table 2: Observation parameters for each object in the sample. Columns (1), (2) and (3) give the object name, observation ID and observation start date, respectively. The XIS detectors used in the observation are shown in column (4). Column (5) gives the combined exposure for all available XIS detectors. Source, background and PIN (source plus background) counts are given in columns (6), (7) and (8), respectively. Source and background counts are quoted for all combined XIS detectors. Column (9) gives the source detection level over the background (per cent) in the PIN, where values marked with an asterisk (*) are below the significant detection threshold of 5 per cent. AGN with PIN data with a significance less than 1 per cent, or AGN where no PIN data was available, are marked with a dash.

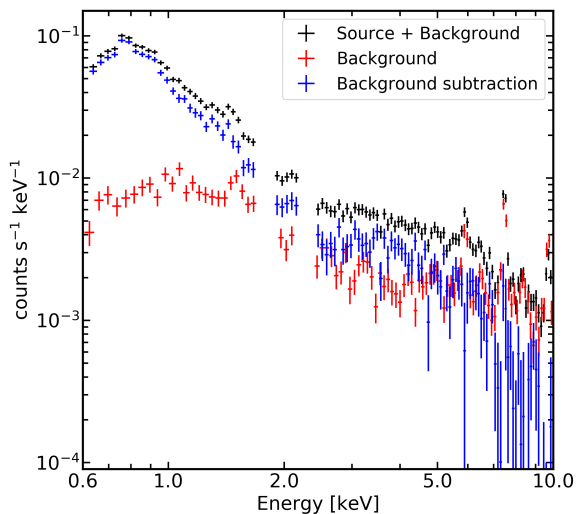


Figure 1. Source+background (black), background (red) and background subtracted spectrum (blue) for a NLS1, 1H0707-495. The background emission lines begin to dominate the spectrum above 6 keV, but the source contribution is still detectable. The source contribution above 6 keV can be better constrained by modelling the background rather than subtracting it or cutting the spectrum.

The background model for each source is constructed using narrow emission features to model the instrumental lines from the detectors and multiple power law components to match the shape of the background continuum. The resulting background models are then applied to the combined source+background spectrum before modelling the source contribution.

4.2 Broad-band model

The goal of this work is not to assume and test a physical model, but instead to characterise the shape of the spectrum and compare important values within the sample. To characterise the shape of the X-ray spectrum, we use a simple toy model. Not all of the AGN spectra are perfectly fit with the toy model, but the spectral shape is sufficiently well measured to allow for comparison.

The model consists of a power law to account for emission from the corona, and a blackbody component to model the soft excess below ~ 2 keV. We also model Fe $K\alpha$ emission with a Gaussian emission profile, with the energy frozen to 6.4 keV and the width frozen to 1 eV so that only the normalisation is free to vary.

To approximate the hard excess emission that might arise from the Compton hump peaking at ~ 20 keV, we use a second Gaussian emission profile, with the width fixed to 5 keV and the energy frozen to 20 keV. We do so because the hard excess is constrained only by the PIN data, which has poorer statistics compared to the XIS data. More complicated models that extend over a broad energy band are dominated by the statistics in the XIS band, which results in the hard excess being improperly modelled for some sources. The Gaussian model is sufficient to approximate the shape of the hard excess and it improves spectral modelling.

This model is modified by both Galactic absorption as well as an additional absorption component, redshifted to the host galaxy frame. In XSPEC, the source model is employed as TBABS \times ZT-

BABS(ZGAUSS + ZGAUSS + BLACKBODY + POWERLAW). For each object, the individual background model is also applied to the spectrum to form the total model. For each AGN in our sample, model parameters are given in Table 3.

To illustrate this modelling process, the top panel of Fig. 2 shows the XIS source+background (black), XIS background (red), and PIN (gray) spectra unfolded against a power law with $\Gamma=0$ for the BLS1 galaxy Ark 120. A similar figure has been prepared for each source, and these are included as supplementary online material. The data have been redshift corrected for ease of interpretation. The background increases significantly at higher energies. Several instrumental lines are also seen in the background spectrum, including strong features at 6.5, 7.5 and 9.7 keV (see Tawa et al. 2008). These features, especially the line at 9.7 keV, are strong enough to be seen in the source+background spectrum.

The second panel shows the residuals (data/model) for the background model applied to the background spectrum. This model is comprised of multiple power law and Gaussian components to fit the observed curvature. No clear residuals can be seen, and the background data are well fit. In the third panel, we show the residuals for a power law model applied to the background modelled spectrum, fit between 2 – 4 and 7 – 10 keV and extrapolated to all energies. A strong soft excess below 2 keV, Fe $K\alpha$ emission between 5 – 7 keV, and a hard excess peaking at 20 – 25 keV are visible. Finally, the bottom panel presents the residuals to our toy model applied to the background modelled XIS data and the PIN data. Aside from some remaining curvature in the 5 – 7 keV band on either side of the narrow Fe $K\alpha$ line at 6.4 keV, the X-ray continuum appears to be reasonably approximated.

We select a number of parameters of interest for further study. These include the host galaxy absorption column density (znH), the blackbody temperature (kT), the photon index (Γ), and the 3 – 10 keV unabsorbed luminosity (L_x). We also approximate the Eddington ratio using the ratio of X-ray luminosity to the Eddington luminosity, L_x/L_{Edd} , which we call the X-ray Eddington ratio (see Section. 4.3).

Since *Suzaku* has the capability to simultaneously observe the soft and hard excesses, measuring these parameters is of great interest. We therefore define the soft excess strength, SE, as the ratio of the (unabsorbed) blackbody luminosity to the power law luminosity in the 0.6 – 1.5 keV band:

$$\text{SE} = \frac{\text{BB}_{0.6-1.5\text{keV}}}{\text{PL}_{0.6-1.5\text{keV}}} \quad (1)$$

The hard excess, HE, is similarly defined as the ratio of the Compton hump luminosity in the 15 – 25 keV band to the power law luminosity in the same energy range:

$$\text{HE} = \frac{\text{CH}_{15-25\text{keV}}}{\text{PL}_{15-25\text{keV}}} \quad (2)$$

Finally, to assess the strength of the narrow Fe $K\alpha$ line relative to the continuum for each object, we define the iron line strength (Fe/L_x) as the ratio of the iron line luminosity to the 3 – 10 keV X-ray luminosity. All parameters will be measured and discussed throughout the remainder of this work.

4.3 The Eddington luminosity

Previous works (e.g. Pounds et al. 1995; Wang et al. 1996; Grupe 2004; Grupe et al. 2010) have shown that on average NLS1 exhibit higher $L_{\text{bol}}/L_{\text{Edd}}$ ratios than BLS1s. Studies with optical spectra of Seyfert 1 galaxies suggest that $L_{\text{bol}}/L_{\text{Edd}}$ may be the driving

(1)	(2)	(3)	(4)	(5)	(6)	(7)	(8)	(9)	(10)
Object	znH [$\times 10^{22}$ cm $^{-2}$]	kT [keV]	Γ	SE	HE	Fe/L $_x$	L $_x$ [erg s $^{-1}$]	L $_x$ /L $_{\text{Edd}}$	C-stat/dof
NLS1									
1H0323+342	< 0.0028	0.134 \pm 0.003	1.90 \pm 0.01	0.65 \pm 0.04	0.21 \pm 0.11	0.0032 \pm 0.001	6.58 $\times 10^{43}$	0.026	392/249
1H0707-495	0.18 $^{+0.68}_{-0.09}$	0.093 \pm 0.005	1.75 \pm 0.09	8.2 $^{+5.5}_{-3.3}$	4.8 \pm 3.5	< 0.016	1.40 $\times 10^{42}$	0.005	280/218
Ark 564	< 0.0006	0.135 \pm 0.001	2.542 \pm 0.008	0.59 \pm 0.01	0.75 \pm 0.02	0.0039 \pm 0.0011	1.94 $\times 10^{43}$	0.081	681/296
IRAS 05262+4432	< 0.048	0.14 \pm 0.01	2.08 $^{+0.04}_{-0.06}$	0.66 $^{+0.29}_{-0.08}$	2.0 \pm 1.8	< 0.00009	2.45 $\times 10^{42}$	0.001	240/208
IRAS 13224-3809	0.10 \pm 0.01	0.104 \pm 0.001	2.22 \pm 0.03	2.6 \pm 0.2	-	< 0.0059	5.99 $\times 10^{42}$	0.007	391/210
MCG-6-30-15	0.320 \pm 0.002	0.0539 \pm 0.0004	1.880 \pm 0.002	0.78 \pm 0.05	0.12 \pm 0.02	0.0067 \pm 0.0004	4.37 $\times 10^{42}$	0.017	2290/368
Mrk 1040	0.451 \pm 0.004	0.048 \pm 0.002	1.926 \pm 0.004	0.33 $^{+0.25}_{-0.14}$	0.45 \pm 0.04	0.0115 \pm 0.001	1.73 $\times 10^{43}$	0.003	665/251
Mrk 110	< 0.0030	0.14 \pm 0.01	1.79 \pm 0.01	0.17 \pm 0.02	0.223 $^{+0.004}_{-0.07}$	0.0064 \pm 0.0015	4.66 $\times 10^{43}$	0.019	308/282
Mrk 335	< 0.00054	0.129 \pm 0.001	1.897 \pm 0.007	0.91 \pm 0.02	0.98 \pm 0.17	0.019 \pm 0.001	9.35 $\times 10^{42}$	0.004	1445/287
Mrk 359	< 0.0037	0.17 $^{+0.01}_{-0.02}$	1.71 $^{+0.03}_{-0.02}$	0.24 \pm 0.03	0.091 $^{+0.003}_{-0.03}$	0.014 \pm 0.003	2.80 $\times 10^{42}$	0.013	270/236
Mrk 478	< 0.0084	0.139 \pm 0.007	2.21 \pm 0.04	0.59 \pm 0.06	1.0 \pm 0.9	< 0.000004	3.02 $\times 10^{43}$	0.012	242/210
Mrk 766	0.207 \pm 0.006	0.062 $^{+0.002}_{-0.001}$	1.813 \pm 0.006	0.66 $^{+0.13}_{-0.11}$	0.262 $^{+0.002}_{-0.08}$	0.008 \pm 0.0014	3.92 $\times 10^{42}$	0.005	528/247
NGC 4051	< 0.00037	0.103 \pm 0.002	1.910 \pm 0.004	0.23 \pm 0.01	0.52 \pm 0.05	0.0141 \pm 0.0007	1.73 $\times 10^{41}$	0.001	1771/295
PG 1211+143	0.06 \pm 0.02	0.080 \pm 0.003	1.79 \pm 0.01	0.74 $^{+0.13}_{-0.11}$	0.05899 $^{+0.34}_{-0.06}$	0.0095 $^{+0.0028}_{-0.0027}$	5.08 $\times 10^{43}$	0.010	346/237
PG 1404+226	0.10 $^{+0.06}_{-0.07}$	0.093 \pm 0.006	1.39 \pm 0.08	4.6 $^{+1.8}_{-1.2}$	12.4 $^{+2.5}_{-2.4}$	< 0.00003	6.39 $\times 10^{42}$	0.011	252/182
PKS 0558-504	< 0.0029	0.130 \pm 0.003	2.21 \pm 0.01	0.43 \pm 0.02	0.42 \pm 0.18	< 0.0022	5.33 $\times 10^{44}$	0.066	299/256
RE J1034+396	< 0.0070	0.113 \pm 0.003	2.34 \pm 0.04	1.7 \pm 0.2	10.7 \pm 2.9	0.0089 $^{+0.0076}_{-0.0071}$	3.24 $\times 10^{42}$	0.010	248/187
RX J0134.2-4258	0.08 \pm 0.02	0.07 \pm 0.02	2.36 \pm 0.02	0.28 $^{+3.12}_{-0.22}$	3.6 \pm 2.9	< 0.0076	2.64 $\times 10^{44}$	0.100	187/171
RX J1633.3+4718	0.61 \pm 0.05	0.101 \pm 0.008	2.12 \pm 0.03	0.95 $^{+0.40}_{-0.26}$	2.1 \pm 1.2	< 0.00002	3.58 $\times 10^{43}$	0.093	261/202
SWIFT J2127.4+5654	0.27 \pm 0.01	0.21 \pm 0.01	1.96 \pm 0.02	0.22 \pm 0.03	0.21 \pm 0.07	0.0069 \pm 0.0016	1.22 $\times 10^{43}$	0.006	310/273
TON S180	< 0.0030	0.135 $^{+0.003}_{-0.004}$	2.31 \pm 0.02	0.48 \pm 0.02	1.5 \pm 0.5	0.0029 \pm 0.0021	3.75 $\times 10^{43}$	0.041	351/241
WKK 4438	< 0.0032	0.25 \pm 0.03	1.90 \pm 0.02	0.091 $^{+0.033}_{-0.034}$	0.029 $^{+0.001}_{-0.009}$	0.0077 $^{+0.0023}_{-0.0022}$	5.34 $\times 10^{42}$	0.021	273/240
BLS1									
1H0419-577	< 0.00068	0.147 \pm 0.003	1.831 \pm 0.007	0.35 \pm 0.01	0.28 \pm 0.05	0.0040 \pm 0.0007	3.40 $\times 10^{44}$	0.021	1012/299
3C 111	0.816 \pm 0.004	< 0.19	1.678 \pm 0.003	0.0024 $^{+0.006}_{-0.0002}$	0.00226 $^{+0.00001}_{-0.0007}$	0.0050 \pm 0.0005	1.97 $\times 10^{44}$	0.0004	645/303
3C 120	< 0.00053	0.168 \pm 0.006	1.817 \pm 0.005	0.147 \pm 0.007	0.13 \pm 0.02	0.0080 \pm 0.0005	9.27 $\times 10^{43}$	0.014	1008/274
3C 382	< 0.0017	0.091 \pm 0.004	1.808 \pm 0.004	0.16 \pm 0.03	0.0385 $^{+0.0002}_{-0.01}$	0.0059 \pm 0.0007	2.61 $\times 10^{44}$	0.003	486/300
3C 390.3	< 0.0028	0.152 \pm 0.007	1.709 \pm 0.008	0.19 \pm 0.01	0.0370 $^{+0.0004}_{-0.01}$	0.0071 \pm 0.0009	2.39 $\times 10^{44}$	0.004	371/249
3C 78	0.12 $^{+0.12}_{-0.09}$	0.16 \pm 0.01	2.35 \pm 0.06	0.40 \pm 0.08	-	< 0.0079	1.45 $\times 10^{42}$	0.0001	241/169
4C+74.26	0.05 \pm 0.01	0.05 \pm 0.01	1.811 \pm 0.007	0.11 $^{+2.28}_{-0.09}$	0.28 \pm 0.04	0.0070 \pm 0.0008	6.05 $\times 10^{44}$	0.001	489/258
Ark 120	< 0.0014	0.134 \pm 0.004	1.977 \pm 0.009	0.37 \pm 0.02	0.38 \pm 0.07	0.013 \pm 0.001	5.62 $\times 10^{43}$	0.004	713/294
B3 0309+411	0.06 \pm 0.02	0.07 \pm 0.01	1.81 $^{+0.01}_{-0.02}$	0.39 $^{+1.11}_{-0.26}$	0.0201 $^{+0.0003}_{-0.006}$	0.0056 \pm 0.0028	1.58 $\times 10^{44}$	-	202/200
CBS 126	< 0.011	0.066 \pm 0.004	1.99 \pm 0.01	0.53 $^{+0.27}_{-0.17}$	0.74 \pm 0.42	0.0085 \pm 0.0031	4.87 $\times 10^{43}$	0.006	325/249
ESO 511-G030	< 0.0013	0.134 \pm 0.005	1.778 \pm 0.006	0.22 \pm 0.01	0.22 \pm 0.07	0.0106 \pm 0.0009	1.85 $\times 10^{43}$	0.002	574/258
ESO 548-G081	< 0.012	0.14 \pm 0.02	1.66 \pm 0.02	0.16 $^{+0.06}_{-0.03}$	0.151 $^{+0.004}_{-0.045}$	0.016 \pm 0.003	5.15 $\times 10^{42}$	0.001	257/252
Fairall 9	< 0.00047	0.150 \pm 0.003	1.909 \pm 0.006	0.270 \pm 0.008	0.42 \pm 0.04	0.0143 \pm 0.0007	9.60 $\times 10^{43}$	0.004	1389/283
IGR J16185-5928	< 0.0089	0.16 $^{+0.02}_{-0.03}$	1.88 \pm 0.03	0.206 $^{+0.08}_{-0.04}$	0.80 \pm 0.23	0.0093 $^{+0.0027}_{-0.0026}$	1.72 $\times 10^{43}$	0.006	340/271
IGR J19378-0617	< 0.0016	0.135 \pm 0.003	2.20 \pm 0.01	0.44 \pm 0.02	0.125 $^{+0.002}_{-0.04}$	0.0071 \pm 0.0017	4.06 $\times 10^{42}$	-	492/256

(1)	(2)	(3)	(4)	(5)	(6)	(7)	(8)	(9)	(10)
Object	znH [$\times 10^{22}$ cm $^{-2}$]	kT [keV]	Γ	SE	HE	Fe/ L_x	L_x [erg s $^{-1}$]	L_x/L_{Edd}	C-stat/dof
III Zw 2	< 0.0063	0.18 $^{+0.05}_{-0.13}$	1.58 $^{+0.03}_{-0.02}$	0.07412 $^{+0.81}_{-0.03}$	0.18 \pm 0.13	0.0070 $^{+0.0022}_{-0.0021}$	1.49 $\times 10^{44}$	0.011	242/247
Kaz 102	< 0.016	0.24 $^{+0.06}_{-0.05}$	1.53 \pm 0.03	0.18 $^{+0.13}_{-0.08}$	0.295 $^{+0.009}_{-0.09}$	0.0066 $^{+0.0068}_{-0.0062}$	8.61 $\times 10^{43}$	0.007	205/202
LEDA 168563	< 0.024	0.12 \pm 0.02	1.63 \pm 0.01	0.19 $^{+0.18}_{-0.07}$	0.0704 $^{+0.001}_{-0.02}$	0.0091 \pm 0.0016	2.68 $\times 10^{43}$	0.002	308/244
MCG-02-14-009	< 0.0069	0.15 \pm 0.02	1.79 \pm 0.03	0.28 $^{+0.06}_{-0.04}$	0.56 $^{+0.29}_{-0.28}$	0.014 \pm 0.003	6.09 $\times 10^{42}$	0.004	358/268
MCG-2-58-22	< 0.00095	0.143 \pm 0.008	1.755 $^{+0.006}_{-0.007}$	0.15 \pm 0.01	0.12 \pm 0.03	0.0064 \pm 0.0006	2.32 $\times 10^{44}$	0.006	689/281
MCG+04-22-042	< 0.0044	0.13 \pm 0.01	1.88 \pm 0.02	0.24 $^{+0.06}_{-0.04}$	0.30 $^{+0.19}_{-0.18}$	0.012 \pm 0.003	2.72 $\times 10^{43}$	0.001	290/248
MCG+8-11-11	0.014 \pm 0.003	0.056 \pm 0.008	1.699 \pm 0.004	0.06 $^{+0.15}_{-0.04}$	0.0261 $^{+0.0001}_{-0.008}$	0.0111 \pm 0.0008	4.94 $\times 10^{43}$	0.003	497/296
MR 2251-178	0.11 \pm 0.01	0.059 \pm 0.003	1.649 \pm 0.004	0.29 $^{+0.16}_{-0.10}$	0.00282 $^{+0.00001}_{-0.0008}$	0.0036 \pm 0.0007	3.22 $\times 10^{44}$	0.013	626/283
Mrk 1018	< 0.015	0.16 \pm 0.03	1.80 \pm 0.03	0.14 $^{+0.07}_{-0.03}$	0.52 \pm 0.22	0.0088 $^{+0.0032}_{-0.0031}$	3.39 $\times 10^{43}$	0.004	300/251
Mrk 1148	< 0.013	0.12 \pm 0.01	1.82 \pm 0.02	0.27 $^{+0.10}_{-0.06}$	0.39 \pm 0.18	0.0065 \pm 0.0030	1.26 $\times 10^{44}$	-	251/216
Mrk 1320	< 0.043	< 0.15	1.50 \pm 0.06	< 0.02	-	< 0.00053	2.82 $\times 10^{43}$	-	151/153
Mrk 205	< 0.0071	0.12 \pm 0.01	1.89 \pm 0.02	0.27 $^{+0.06}_{-0.04}$	1.08 $^{+0.17}_{-0.90}$	0.013 \pm 0.002	8.57 $\times 10^{43}$	0.003	397/258
Mrk 279	< 0.0039	0.19 $^{+0.02}_{-0.03}$	1.55 \pm 0.03	0.16 \pm 0.03	0.68 \pm 0.18	0.032 \pm 0.003	8.56 $\times 10^{42}$	0.002	346/264
Mrk 352	< 0.0068	0.11 $^{+0.02}_{-0.03}$	1.79 $^{+0.02}_{-0.03}$	0.19 $^{+0.18}_{-0.07}$	0.102 $^{+0.003}_{-0.03}$	0.011 \pm 0.003	4.90 $\times 10^{42}$	0.004	282/249
Mrk 509	< 0.00019	0.152 \pm 0.005	1.875 \pm 0.006	0.187 $^{+0.007}_{-0.006}$	0.34 \pm 0.03	0.0078 \pm 0.0006	1.06 $\times 10^{44}$	0.008	1980/279
Mrk 530	< 0.0022	0.179 $^{+0.009}_{-0.01}$	1.91 \pm 0.01	0.19 \pm 0.02	0.27 \pm 0.09	0.011 \pm 0.001	3.26 $\times 10^{43}$	0.002	387/242
Mrk 79	0.12 $^{+0.03}_{-0.02}$	0.067 $^{+0.006}_{-0.005}$	1.596 \pm 0.008	0.24 $^{+0.18}_{-0.09}$	0.0134 $^{+0.0001}_{-0.004}$	0.019 \pm 0.002	1.35 $\times 10^{43}$	0.003	429/276
Mrk 841	< 0.00074	0.097 \pm 0.004	1.770 \pm 0.005	0.24 $^{+0.04}_{-0.03}$	0.43 \pm 0.06	0.0145 \pm 0.0009	2.71 $\times 10^{43}$	0.003	1130/283
NGC 4593	< 0.0012	0.063 \pm 0.002	1.695 \pm 0.003	0.18 $^{+0.05}_{-0.04}$	0.13 \pm 0.06	0.0214 \pm 0.0008	2.45 $\times 10^{42}$	0.002	628/278
NGC 6814	< 0.011	< 0.082	1.51 \pm 0.01	0.0351 $^{+0.0006}_{-0.01}$	0.4245 $^{+0.007}_{-0.13}$	0.012 \pm 0.003	5.40 $\times 10^{41}$	0.0002	250/226
NGC 7213	< 0.0065	0.119 \pm 0.009	1.733 \pm 0.007	0.095 $^{+0.019}_{-0.014}$	0.0683 $^{+0.0005}_{-0.02}$	0.012 \pm 0.001	1.42 $\times 10^{42}$	0.0001	456/286
NGC 7469	< 0.0017	0.095 $^{+0.007}_{-0.006}$	1.760 \pm 0.008	0.18 $^{+0.06}_{-0.04}$	0.27 \pm 0.07	0.019 \pm 0.002	9.89 $\times 10^{42}$	0.009	506/282
NGC 985	0.13 \pm 0.04	0.057 $^{+0.005}_{-0.004}$	1.78 \pm 0.01	0.53 $^{+0.51}_{-0.24}$	0.28 \pm 0.19	0.011 \pm 0.003	4.66 $\times 10^{43}$	-	251/248
PG 1322+659	< 0.074	0.08 \pm 0.04	1.95 \pm 0.05	0.29 $^{+9.7}_{-0.24}$	-	< 0.010	4.39 $\times 10^{43}$	0.002	195/161
PG 1626+554	< 0.10	0.15 \pm 0.02	2.05 \pm 0.04	0.27 $^{+0.07}_{-0.05}$	-	0.011 \pm 0.004	1.27 $\times 10^{44}$	0.002	188/168
RBS 1124	< 0.093	0.12 \pm 0.02	1.9 \pm 0.02	0.25 $^{+0.15}_{-0.07}$	0.53 \pm 0.17	0.0044 $^{+0.0027}_{-0.0026}$	4.76 $\times 10^{44}$	0.021	369/267
SBS 1301+540	< 0.069	0.16 \pm 0.02	1.62 $^{+0.02}_{-0.03}$	0.21 $^{+0.05}_{-0.04}$	0.144 $^{+0.005}_{-0.04}$	0.010 \pm 0.003	6.94 $\times 10^{42}$	0.002	281/193
SWIFT J0501.9-3239	< 0.0035	0.107 $^{+0.009}_{-0.008}$	1.89 \pm 0.01	0.16 $^{+0.05}_{-0.03}$	0.27 \pm 0.07	0.011 \pm 0.002	8.56 $\times 10^{42}$	-	371/271
SWIFT J0904.3+5538	0.18 $^{+0.12}_{-0.10}$	0.07 $^{+0.02}_{-0.01}$	1.66 \pm 0.03	0.27 $^{+1.30}_{-0.19}$	0.39 $^{+0.01}_{-0.12}$	0.017 $^{+0.008}_{-0.007}$	1.13 $\times 10^{43}$	-	183/197
SWIFT J1310.9-5553	< 0.15	0.12 $^{+0.04}_{-0.03}$	1.50 \pm 0.02	0.19 $^{+0.32}_{-0.10}$	0.185 $^{+0.005}_{-0.06}$	< 0.0028	1.22 $\times 10^{44}$	-	257/232
UGC 6728	< 0.0035	0.16 \pm 0.01	1.77 \pm 0.02	0.29 \pm 0.03	0.19 \pm 0.16	0.0091 $^{+0.0027}_{-0.0026}$	1.06 $\times 10^{42}$	0.002	310/251
ZW 229-15	< 0.0042	0.16 $^{+0.01}_{-0.02}$	1.74 \pm 0.03	0.25 \pm 0.03	-	0.013 \pm 0.003	5.66 $\times 10^{42}$	0.006	480/224

Table 3: Toy model parameters and associated errors. Object names are given in column (1). Host galaxy column densities (znH) are given in column (2) in units of 10^{22} cm $^{-2}$. The blackbody temperature (kT) and photon index (Γ) are given in columns (3) and (4), respectively. Columns (5), (6), and (7) give the soft excess (SE), hard excess (HE) and iron line strength (Fe/ L_x), respectively. Error bars on the soft and hard excesses have been computed using error propagation of the blackbody, powerlaw and Compton hump luminosities. The 3 – 10 keV luminosities are given in column (8), and the X-ray Eddington ratios (L_x/L_{Edd}) are given in column (9). Column (10) gives the fit quality, in terms of the C-stat over the degrees of freedom (dof).

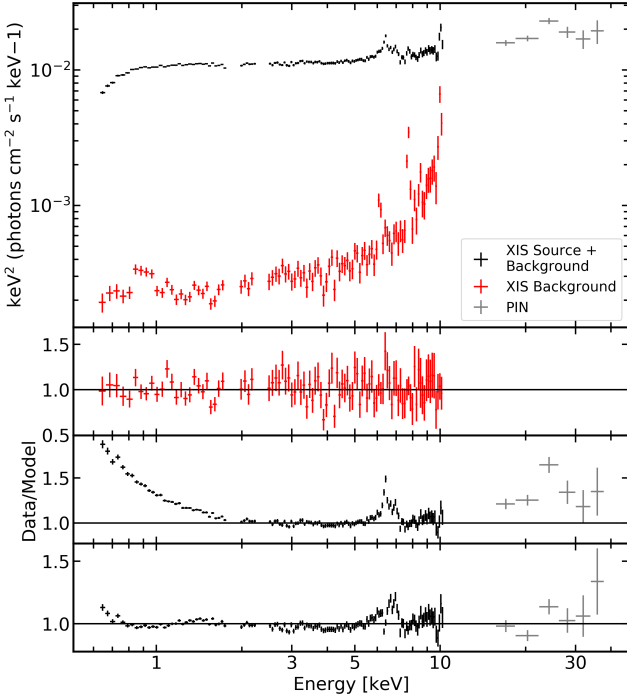


Figure 2. Top panel: XIS source+background (black), XIS background (red), and PIN (gray) spectra unfolded against a power law with $\Gamma=0$. The background increases toward higher energies. Second panel: residuals (data/model) for the background model. No clear residuals are present. Third panel: residuals for a power law model applied to the background modelled spectrum, fit between 2 – 4 and 7 – 10 keV and extrapolated to lower and higher energies. A strong soft excess below 2 keV, Fe $K\alpha$ emission from 5 – 7 keV, and a hard excess peaking at 20 – 25 keV are visible. Bottom panel: residuals for the toy model applied to the data. Some residuals are present on either side of the narrow Fe $K\alpha$ line, but the spectrum is otherwise well approximated. All spectra have been redshift corrected.

mechanism behind the so-called eigenvector 1, the primary axis of variance between the two classes (Boroson & Green 1992). It is therefore of great interest to properly characterise this value.

Many works suggest that the bolometric luminosity can be calculated using the X-ray luminosity with a scaling factor ranging from ~ 5 to ~ 100 , depending on various host galaxy and AGN properties (e.g. Lusso et al. 2010, 2012). There are also indications that the ratio of $L_{\text{bol}}/L_{\text{Edd}}$ may be closely linked with the photon index of the power law component, Γ (e.g. Shemmer et al. 2008; Brightman et al. 2013).

To investigate this, we use two different methods to approximate the Eddington ratio. The histograms for these distributions, shown for the entire sample of NLS1 and BLS1 galaxies, is presented in Fig. 3. In the first we use the X-ray luminosity to approximate the bolometric luminosity, scaled by a factor of 10 (purple solid line). In the second, we use equation (2) of Brightman et al. (2013), which gives the relationship between Γ and $L_{\text{bol}}/L_{\text{Edd}}$ (black dashed lines). For some individual sources, there can be large discrepancies, however the two methods give very similar distributions and median values, suggesting that L_x/L_{Edd} is a reasonable proxy for $L_{\text{bol}}/L_{\text{Edd}}$. Throughout the remainder of this work, we define this ratio of X-ray luminosity to Eddington luminosity, L_x/L_{Edd} , as the X-ray Eddington ratio. This is advantageous so that we can continue to treat photon index and L_x/L_{Edd} independently and compare them in Section 5.

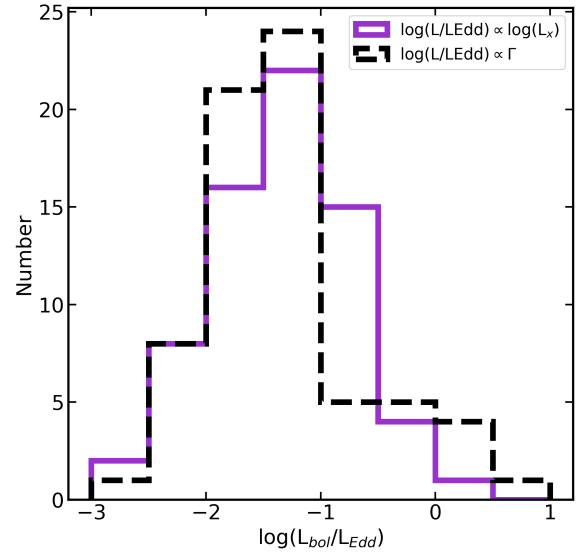


Figure 3. Comparison of methods for calculating the Eddington luminosity ratio, shown for the entire sample. The purple solid line shows the Eddington ratio estimated as $10 \times L_x/L_{\text{Edd}}$, while the black dashed line shows the calculation using the Γ – $L_{\text{bol}}/L_{\text{Edd}}$ relationship of Brightman et al. (2013). The two distributions are in close agreement, supporting the use of L_x/L_{Edd} to approximate the Eddington luminosity ratio for further analysis.

Fig. 4 shows the distributions of L_x/L_{Edd} for NLS1 and BLS1 galaxies, shown in log space for ease of interpretation. NLS1 galaxies are shown as blue solid lines and BLS1 galaxies are shown as red dashed lines. The median values for each parameter are shown as vertical lines in corresponding colours and line styles. We find that NLS1 galaxies show higher median L_x/L_{Edd} , with a median value of $\log(L_x/L_{\text{Edd}}) = -1.94$ (corresponding to $L_x/L_{\text{Edd}} = 0.01$) for NLS1 galaxies compared to $\log(L_x/L_{\text{Edd}}) = -2.49$ (corresponding to $L_x/L_{\text{Edd}}=0.003$) for BLS1 galaxies.

To assess the similarity of the distributions, we compute the Kolmogorov-Smirnov (KS) test on the two samples. This test compares two samples to compute the statistical likelihood that they are drawn from the same parent population. The KS test, implemented in PYTHON using SCIPY.STATS.KS_2SAMP(), returns a KS test statistic and a p-value. If the KS statistic is large (p-value is small), we can reject the null hypothesis that the two samples are drawn from the same distribution. For the ratio of L_x/L_{Edd} , we compute a p-value of 0.00038, implying that the samples are different at above the 99.9 per cent confidence level.

4.4 Parameter distributions

Upon obtaining all the relevant parameters from the model, it is of interest to compare the distributions of each of these parameters between the NLS1 and BLS1 galaxies to search for similarities and differences between the two samples. All such distributions are presented in Fig. 5. In each panel, the histogram for NLS1 galaxies is shown as a blue solid line, and the BLS1 histogram is shown as a red dashed line. The median values for each parameter are shown as vertical lines in corresponding colours and line styles, and median values are given in the label for each plot.

First, panel (a) presents the luminosity distributions of the two samples, shown as $\log(L_x)$ in the 3 – 10 keV range. This band was selected to avoid any effects of absorption or contributions from the soft excess, which may have complicated a direct comparison

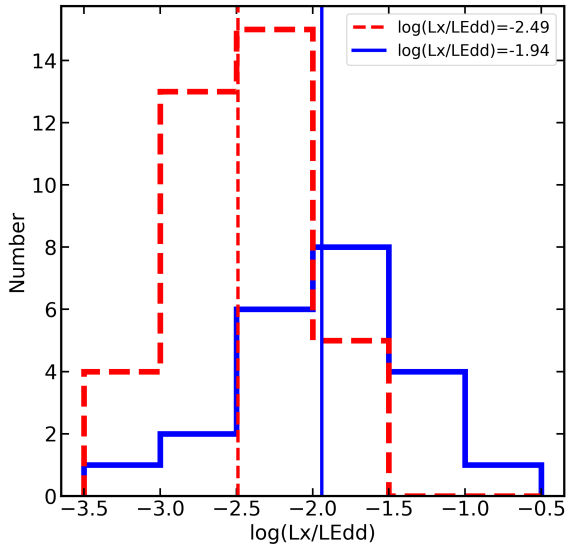


Figure 4. Distribution of $\log(L_x/L_{\text{Edd}})$ for NLS1 and BLS1 galaxies, where the NLS1 parameter values are shown in blue solid lines and BLS1 parameter values are shown as red dashed lines. The median values for each parameter are shown as vertical lines in corresponding colours and line styles. As expected, NLS1 galaxies show evidence for higher X-ray Eddington ratios (KS test p-value 0.00038).

between sources. The distributions show that a suitable range of luminosities are covered between the two samples. The NLS1 luminosities have a lower median value ($\log(L_x)=43.03$ compared to $\log(L_x)=43.53$ for BLS1 galaxies), likely owing to their lower black hole masses. We have also performed the KS test on the redshift distributions, and the measured p-value of 0.8 shows that no differences within the sample are attributable to redshift. The symmetry of the distributions suggests that the sample is largely unbiased in luminosity and covers a sufficient scope of type-1 AGN. From the KS test, we compute a p-value of 0.12, indicating that the distributions are similar.

Panel (b) shows the distributions of host-galaxy absorption (znH), again shown in log space. Many of these values are upper limits, as many galaxies showed little to no clear evidence for absorption within the *Suzaku* bands. When only an upper limit is present, the upper limit is shown in the histogram. We note also that very low absorption values of $10^{18} - 10^{19} \text{ cm}^{-2}$ are very difficult to constrain given the limited *Suzaku* bandpass at low energies, and should thus be interpreted with caution. While the median level for absorption appears slightly higher for NLS1 galaxies, the KS test returns a p-value of 0.27, implying that the distributions are not statistically different.

Many of these parameters include large errors, so we have attempted to quantify the confidence range for the KS test results. To do so, we take each parameter for each source and draw a perturbed value based on a normal distribution, centred on the parameter value and extending to the upper and lower error bars. This process is repeated 10000 times, and the p-value calculated for each perturbed sample. By taking the 5th and 95th percentile values, a range of p-values is obtained. For znH, we find a range of 0.16 – 0.37. This shows that even when considering errors, no statistical differences in the distributions can be found. The same procedure is used to report a confidence range for the p-values for each of the remaining model parameters. This will be given along with measured value based on the best-fit.

Panel (c) shows the distribution of photon index (Γ) values. We note that some sources show very flat Γ values of 1.4 – 1.6; these may potentially be artificially flattened due to the presence of some underlying absorption or reflection component. The median Γ value is significantly higher for NLS1 galaxies, with a p-value of 0.00040 (0.00037 – 0.013) implying > 99.9 per cent confidence. More commonly, average values of the photon index are reported, so to ease comparison with other works, we determine the average values in our sample to be $\Gamma = 1.78 \pm 0.02$ for the BLS1 galaxies and $\Gamma = 2.00 \pm 0.06$ for the NLS1 sample. These are reasonably comparable to the canonical values of ~ 1.9 and ~ 2.1 (e.g. [Nandra & Pounds 1994](#); [Vaughan et al. 1999](#); [Reeves & Turner 2000](#)) that are often adopted. The difference could be attributed to systematic differences between telescopes (e.g. [Ishida et al. 2011](#); [Kettula et al. 2013](#)); but more importantly, our sample confirms the well-known result that NLS1s possess steeper photon indices.

In panel (d), we present the distribution of blackbody temperatures (kT), in units of keV. The distributions are statistically similar, with a p-value of 0.19 (0.087 – 0.38). However, we find that many AGN have kT values around ~ 0.05 keV, compared to more typical values of $\sim 0.10 - 0.15$ keV (e.g. [Mateos et al. 2010](#)). To check if this is an effect of the absorption component, panel (e) shows the same histogram, but including only the sources with upper limits on the absorption component (i.e., sources where the host-galaxy absorption agrees with 0). The median values are now nearly identical for NLS1 and BLS1 galaxies (p-value 0.40; 0.21 – 0.65), and many of the lowest kT sources have been removed, suggesting some degeneracy between these components.

Panels (f), (g) and (h) present the distributions of the iron line strength (Fe/L_x), soft excess strength (SE; shown in log values), and hard excess strength (HE; shown in log values), respectively. For Fe/L_x , NLS1 galaxies exhibit lower median values than BLS1 galaxies (p-value 0.028; 0.0048 – 0.065). By contrast, NLS1 galaxies have stronger median soft excesses and hard excesses than BLS1 galaxies. These differences appear significant in both cases, with p-values of 8.0×10^{-6} ($7.9 \times 10^{-7} - 1.5 \times 10^{-5}$) and 0.0098 (0.0018 – 0.013) for the SE and HE distributions, respectively. The soft excess histogram (panel g) is particularly striking, with the median value for the NLS1 galaxies lying above the value of any BLS1 galaxy. The BLS1 galaxy with a very weak soft excess is 3C 111, a source which shows a very high level of host-galaxy absorption (e.g. [Ballo et al. 2011](#)). Our analysis of this source gives $\log(\text{znH})=21.9$, just below our sample cutoff of 22.0.

The KS test results and distributions show that NLS1 galaxies have steeper photon indices and higher X-ray Eddington ratios with confidence above the 99.9 per cent level, well known results from previous studies (e.g. [Pounds et al. 1995](#); [Boller et al. 1996](#); [Brandt et al. 1997](#); [Leighly 1999](#); [Gierliński & Done 2004](#); [Grube 2004](#); [Crummy et al. 2006](#); [Ojha et al. 2020](#)). The KS test also suggests that NLS1 galaxies exhibit stronger soft excesses than their BLS1 counterparts. Even when considering the p-values based on parameter uncertainties, this difference is significant at the 99.99 per cent confidence level and is the most statistically significant difference between NLS1 and BLS1 galaxies in our sample. This has been observed in various works, although all using slightly differing definitions of the soft excess strength (e.g. [Boller et al. 1996](#); [Vaughan et al. 1999](#); [Grube et al. 2010](#); [Gliozzi & Williams 2020](#)). We also find that the hard excess is stronger in NLS1 galaxies, at the > 99 per cent level. There is also some evidence that the iron strength is weaker in NLS1 galaxies, at the 95 per cent confidence level. This suggests that the differences in the X-ray spectra in NLS1 and BLS1 galaxies go far beyond their power law slopes.

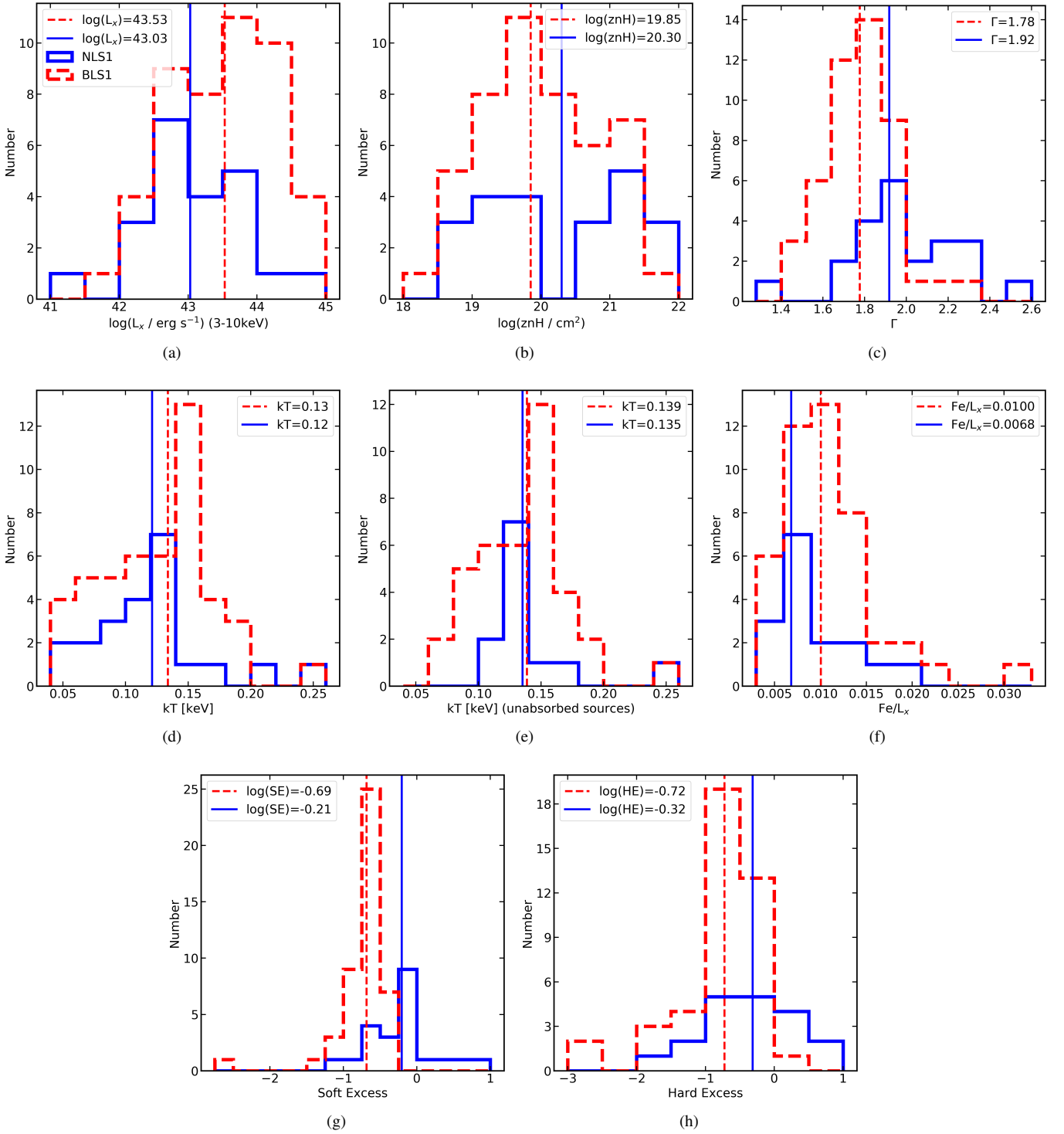


Figure 5. Histograms showing parameter distributions, where the NLS1 parameter values are shown in blue solid lines and BLS1 parameter values are shown as red dashed lines. The median values for each parameter are shown as vertical lines in corresponding colours and line styles, and median values are given in the label for each plot. Panel (a) shows the X-ray luminosity, L_x (3–10 keV) in log space (KS test p-value 0.12); (b) shows host-galaxy absorption in log values (p-value 0.27); (c) shows photon index, Γ (p-value 0.00040). Panel (d) shows black body temperature, kT (p-value 0.19). To show the influence of absorption on the temperature panel (e) shows the kT distribution only for sources that the absorption (znH) is an upper-limit consistent with zero. Many of the low kT objects are missing from this comparison, but the medians are very similar between samples (p-value 0.40). Panel (f) shows iron line strength, Fe/L_x (p-value 0.028); (g) shows soft excess strength on a log-scale, $\log(SE)$ (p-value 8.0×10^{-6}); and (h) shows the hard excess on a log-scale, $\log(HE)$ (p-value 0.0098).

5 SAMPLE ANALYSIS

5.1 Correlation analysis

The next step of our analysis is to search for correlations between the various parameters. We present this analysis in the form of a correlogram, constructed using the function `CORRLOT` implemented in R. This technique fits each pair of parameters and reports the Pearson correlation coefficient, r , obtained from the linear fit. Values of the correlation coefficient of larger than 0.5 indicate a significant positive correlation, while values less than -0.5 indicate a significant anti-correlation.

The result of the correlation analysis for the entire Seyfert sample is shown in Fig. 6. The colour bar at the bottom shows the Pearson correlation coefficient, r , for each pair of parameters; yellow ellipses indicate anti-correlations, while purple indicates positive correlations. Higher ellipticity represents a tighter correlation. To help show which correlations are significant, the r value is also printed on each ellipse.

We use eleven parameters in the analysis; the eight parameters discussed in the previous Section (namely znH , kT , Index (Γ), SE, HE, Fe/L_x , L and L_x/L_{Edd}), as well as the blackbody luminosity in the 0.6 – 1.5 keV band (BB), the Compton hump luminosity in the 15 – 25 keV band (CH), and the iron line luminosity (Fe). The analysis reveals nine significant correlations including three with the X-ray Eddington ratio L_x/L_{Edd} (BB, CH, and Index); three with L_x (BB, CH, and Fe); two others with CH (Fe and BB); and between SE and HE. Most of these correlations are associated with variations in luminosity of some component within the sample, thus it may be expected. For example, brighter AGN typically have higher blackbody, Compton hump, and iron line luminosities. Although not significant, there are also weak anti-correlations between the iron line strength and L, as well as the iron line strength and L_x/L_{Edd} , in agreement with the X-ray Baldwin effect; an anti-correlation between the equivalent width of the Fe $K\alpha$ line and the luminosity of the AGN (e.g. *Iwasawa & Taniguchi 1993*).

The correlation between Γ and the Eddington ratio is well known and has been studied in many works (e.g. *Shemmer et al. 2008; Brightman et al. 2013; Ojha et al. 2020*). This relationship can be explained by considering a link between the Eddington ratio and the X-ray emitting corona. For systems accreting at a higher fraction of their Eddington limit, more emission from the disc will be incident upon the corona, resulting in more Compton up-scattering that causes the corona to cool more quickly. These cooler coronae then produce steeper photon indices (*Pounds et al. 1995*).

The tight correlation between the soft and hard excess components, SE and HE (defined as the ratio of blackbody and Compton hump luminosities, respectively, to the power law luminosity) is less well studied empirically. A hint at such a correlation was considered in *Vasudevan et al. (2014)*, but using different definitions for the soft and hard excess strengths and non-simultaneous observations of the soft and hard energy bands. This result is therefore worthy of further consideration.

To search for differences between NLS1 and BLS1 galaxies, we perform the same analysis separately on the NLS1 and BLS1 samples. The results are shown in Fig. 7. The correlations for NLS1 galaxies are shown in blue, and those for BLS1 galaxies are shown in red. The colour bars below each image show the range of r values for different colours, and the r value for each correlation is printed over the corresponding ellipse.

A comparison between the separate correlograms in Fig. 7 with the correlogram for the entire sample in Fig. 6, shows that

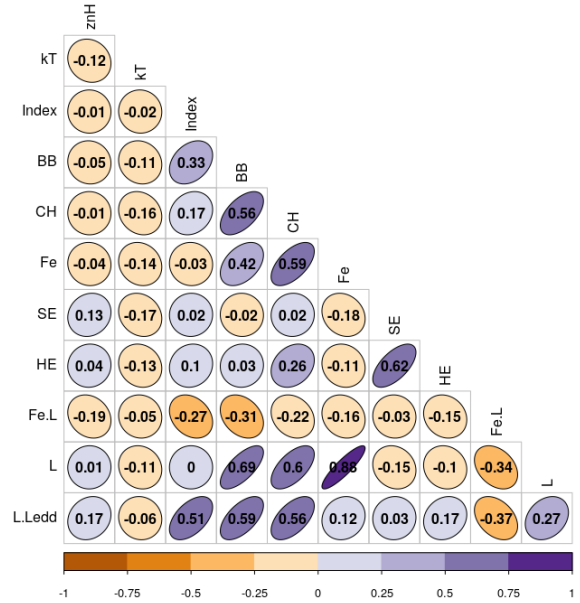


Figure 6. Correlation plots for the complete NLS1 and BLS1 sample. Yellow ellipses indicate anti-correlations, while purple indicates positive correlations. The Pearson correlation coefficient (r) values are written on the ellipses in black. We use eleven parameters in the analysis: host-galaxy column density (znH), blackbody temperature (kT), photon index (Index), blackbody luminosity in the 0.6 – 1.5 keV band (BB), Compton hump luminosity in the 15 – 25 keV band (CH), iron line luminosity (Fe), soft excess strength (SE), hard excess strength (HE), iron line strength (Fe.L), 3–10 keV luminosity (L), and X-ray Eddington ratio (L.Ledd). The analysis reveals nine significant positive correlations ($r > 0.5$).

some trends are stronger in the individual samples than in the total sample. Specifically, the relation between iron line (Fe) and blackbody (BB) luminosities is rather significant in the individual samples ($r \approx 0.72$) and only moderately important in the full sample analysis ($r = 0.42$). Likewise, L_x and L_x/L_{Edd} are significantly correlated in the individual samples ($r \approx 0.54$), but only mildly correlated in the full analysis ($r = 0.27$). The straightforward explanation is that both the NLS1 and BLS1 samples exhibit a similar trend, but are slightly offset as their average luminosities are marginally different (Fig. 5). When combining the two samples the slight differences degrade the overall correlation.

There are also four correlations which are significant in one sample, but not the other. These are highlighted in the correlograms (Fig. 7), and shown in Fig. 8, where NLS1 galaxies are shown as blue circles and BLS1 galaxies are shown as red squares. Upper limits are indicated with arrows. First, in the top left panel (a), BLS1 galaxies show a significant positive correlation between the soft excess strength and photon index (SE and Index). The soft excess is shown on a log axis to show the large range of values.

For NLS1 galaxies, there is an anti-correlation between these parameters, although it is of lower significance with an r value of -0.33. Examining the NLS1 points in panel (a) shows that this anti-correlation for NLS1 galaxies is driven by two sources with strong soft excesses and very flat Γ . These objects are 1H0707-495 and PG 1404+226. Both sources have poor data quality and extremely strong soft excesses. In particular, 1H0707-495 shows extreme spectral complexity in observations with *XMM-Newton* (e.g. *Boller et al. 2002; Gallo et al. 2004; Fabian et al. 2012*), likely indicating the presence of additional absorption or reflection. It is

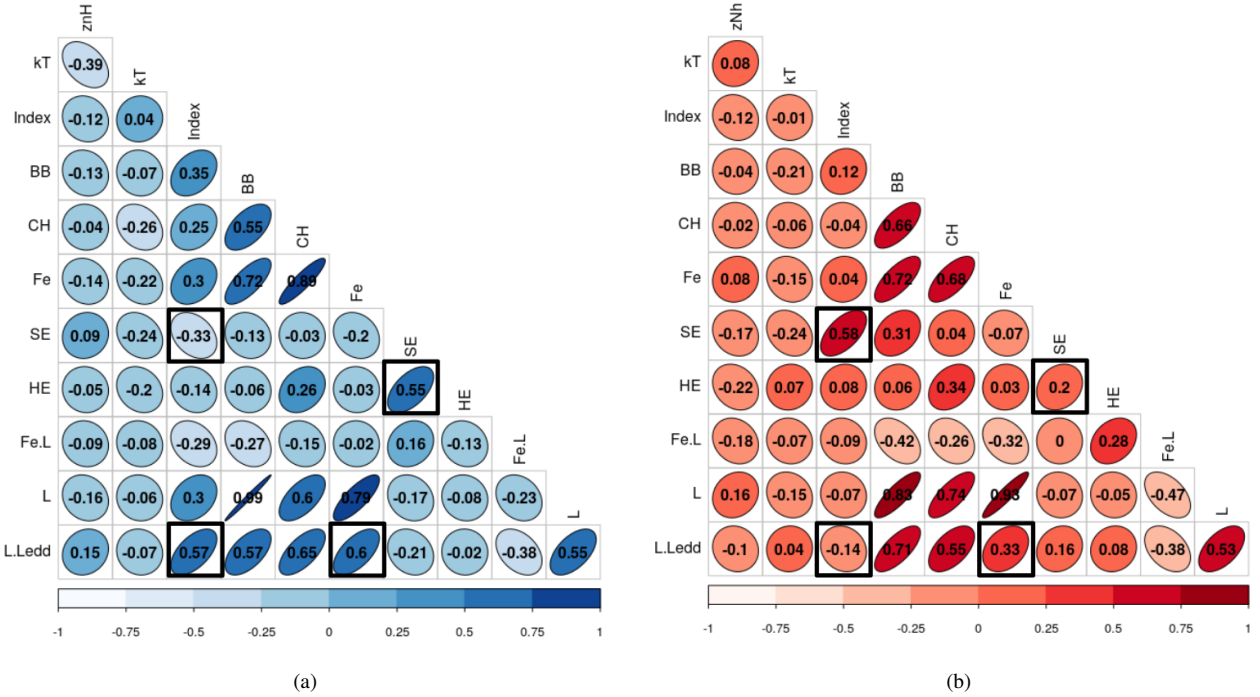


Figure 7. Correlation analysis performed separately for NLS1 (left: blue) and BLS1 (right: red) galaxies. The colour bars at the bottom of each image show the corresponding r values, and these are printed on each ellipse. Column and row names are the same as in Fig. 6. Two correlations, L with L_x/L_{Edd} and Fe with BB, are significant for the individual classes, but not for the full sample. Four correlations are significant in one sample, but not the other; these cells are outlined in black. BLS1 galaxies show a significant positive correlation between the soft excess strength and photon index (SE and Γ), while this correlation is weakly anti-correlated for NLS1 galaxies. The photon index Γ and the iron line luminosity (Fe) are both significantly positively correlated with the X-ray Eddington ratio (L_x/L_{Edd}) for NLS1 galaxies, but not for BLS1 galaxies. Finally, the soft excess and hard excess (SE and HE) are significantly positively correlated for NLS1 galaxies, but not for BLS1 galaxies.

therefore possible that these measured Γ values are not representative of the true underlying continuum. Removing these two outliers diminishes the negative trend but does not result in a significant correlation for the NLS1 sample. To preserve the size and scope of the sample, these objects are kept in the sample for the remainder of this work.

The other three panels show correlations which are significant for NLS1 galaxies, but not for the BLS1 sample. Panel (b) shows the relationship between Γ and L_x/L_{Edd} , where the X-ray Eddington ratio is shown on a log axis for clarity. NLS1 galaxies show a clear positive correlation, while the BLS1 galaxies do not show a significant trend. This is again likely affected by outliers, as both 3C 78 and PG 1626+554 have very low X-ray Eddington ratios but very steep photon indices. These spectra both have poor data quality, and 3C 78 also shows evidence for significant absorption, which may lead to poor measuring of these parameters. A positive correlation is more apparent, in agreement with previous works (e.g. Shemmer et al. 2008; Brightman et al. 2013; Ojha et al. 2020), if these sources were removed.

Panel (c) shows the relationship between the iron line luminosity and L_x/L_{Edd} . Both values are shown on log scales for clarity. There appears to be more scatter in the distribution for BLS1 galaxies, which explains the slightly lower correlation coefficient for BLS1 galaxies ($r = 0.33$) compared to NLS1 galaxies ($r = 0.60$). The correlations appear rather similar in slope, but there is a clear shift in the measured luminosity of the narrow iron line with BLS1 galaxies exhibiting more luminous lines than NLS1 galaxies at a

given L_x/L_{Edd} . This also explains the insignificant correlation that was found between these parameters in the full sample (Fig. 6).

Panel (d) shows the relationships between the soft excess (SE) and hard excess (HE) strengths over the power law. The AGN that do not have PIN data have not been included, as no hard excess could be measured. Both values are shown on log scales to better show the range of values, which span several orders of magnitude. For NLS1 galaxies, a very clear positive trend between these two values is observed. NLS1 galaxies with stronger soft excesses also show stronger hard excesses. The trend observed in the full sample seems therefore to be driven by the NLS1 sample. Neither the soft excess nor hard excess is highly correlated with L_x , which suggests that this relationship cannot be attributed to variations in luminosity. The correlation between these two parameters may instead point to a common origin between the soft excess and hard excess for NLS1 galaxies.

This correlation between SE and HE is not observed for BLS1 galaxies, with a low correlation coefficient of $r = 0.20$. As in the histograms presented in Fig. 5, we observe that 3C 111 is an outlier, with extremely weak soft excess (likely due to large amounts of absorption) and only an upper limit placed on the hard excess. Aside from this source, the distribution of soft excesses is very narrow despite a wide range of hard excesses, spanning a factor of ~ 10 in BLS1s compared to a factor of ~ 100 in NLS1s. Further discussion is given in Section 6.

Finally, it is of interest to note that, although not highly significant in our sample, we do observe anti-correlations between the iron line strength (Fe/L_x) and the X-ray luminosity (L_x), as well

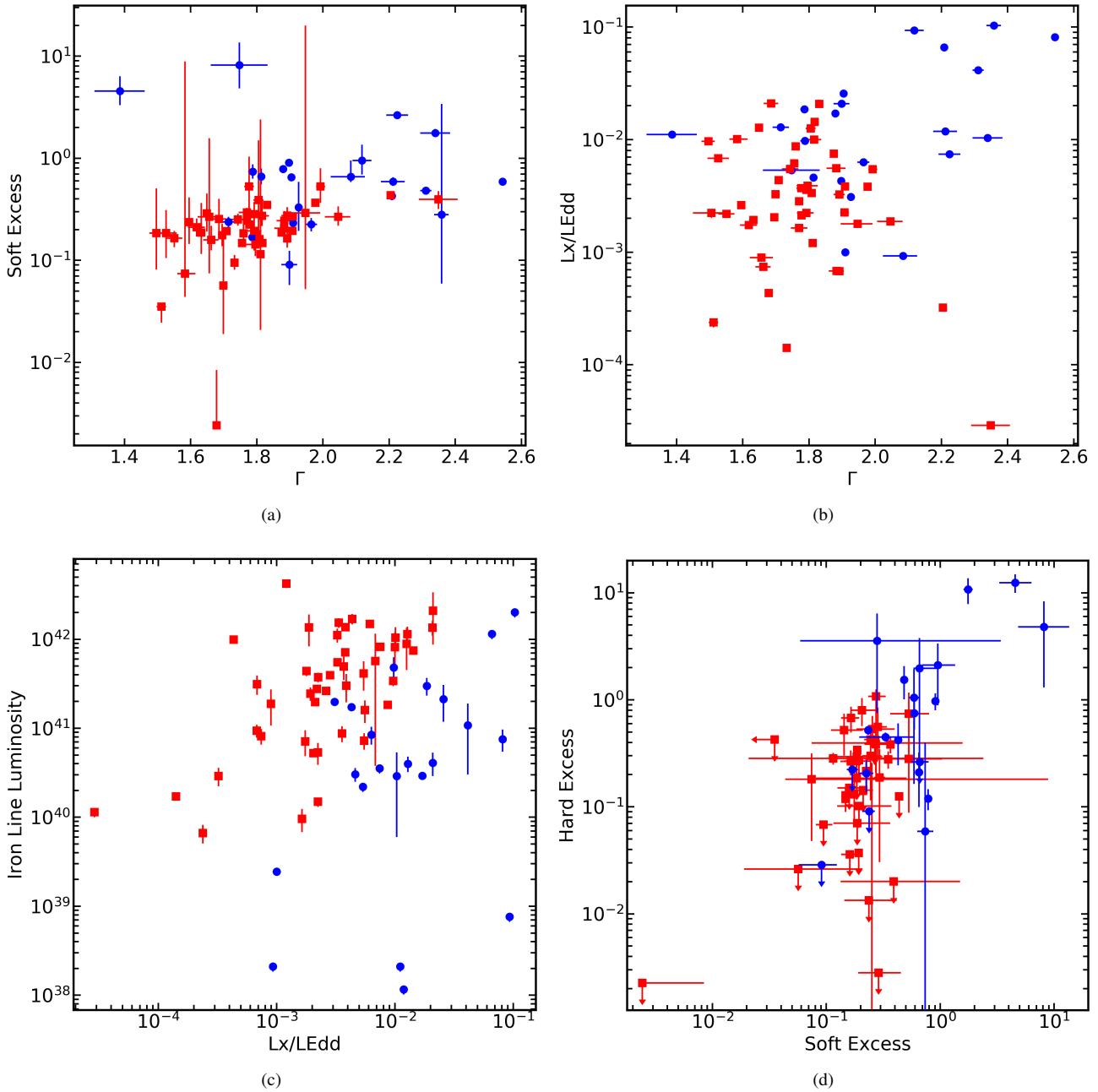


Figure 8. Correlations for NLS1 (blue circles) and BLS1 (red squares) galaxies which are only significant for one sample. Upper limits on measurements are indicated with arrows. Panel (a) shows the distribution of Γ with soft excess strength. The two extreme outliers for NLS1 galaxies are 1H0707-495 and PG 1404+226, two AGN whose extreme spectral curvature and poor data quality may contribute to poor measurement of these values. Panel (b) shows the correlation between Γ and L_x/L_{Edd} . A strong positive correlation is apparent for NLS1 galaxies, while outliers skew the distribution for BLS1 galaxies. Panel (c) shows the correlation between iron line luminosity and L_x/L_{Edd} , with both axes shown in log scale for clarity. The correlation is strong for NLS1 galaxies, but weaker for BLS1 galaxies. Panel (d) shows the relationship between the soft excess and hard excess strengths, both shown in log scale. The correlation is strong for NLS1 galaxies, while BLS1 galaxies do not show any apparent correlation.

as the X-ray Eddington ratio (L_x/L_{Edd}) in both samples. In particular, for BLS1 galaxies, the r value for the correlation between Fe/L_x and L_x is -0.47, very close to our definition of significant. This suggests that the X-ray Baldwin effect is an important feature in our sample, especially for BLS1 galaxies.

5.2 Principal Component Analysis

To better understand the variations between objects in our sample, we employ principal component analysis (PCA). This technique uses eigenvalue decomposition to find the components that contribute to the maximum variations in a data set. We use the package `PRCOMP` in R to perform this analysis. As the correlation plots revealed many tight correlations between the luminosity

(1)	(2)	(3)	(4)	(5)
Parameter	Name	PC1	PC2	PC3
kT	kT	0.0187	0.0401	0.4214
Gamma (Γ)	Index	0.2058	0.0217	0.1970
Soft excess (SE)	SE	0.0625	0.3913	0.0026
Hard excess (HE)	HE	0.1270	0.3062	0.0003
Fe/ L_x	Fe.L	0.2194	0.0507	0.0027
L_x	L	0.0623	0.1485	0.3605
L_x/L_{Edd}	L.Ledd	0.3043	0.0416	0.0154

Table 4. Fractional contributions of each parameter to the first three principal components. Column (1) gives the parameter name, column (2) gives the name as displayed in panel (b) of Fig. 9, column (3) gives the fractional contribution to PC1, column (4) gives the contribution to PC2, and column (5) gives the contribution to PC3. Fractional contributions larger than ~ 0.15 are considered important and are shown in bold.

of the AGN in different energy bands (as expected), we remove the blackbody, Compton hump and iron line luminosities, leaving only the 3–10 keV luminosity (L_x). We also remove the absorption parameter, $z\text{NH}$. This leaves seven parameters for the analysis: kT, Γ , SE, HE, Fe/ L_x , L_x and L_x/L_{Edd} , and thus our data has seven principal components.

First, we compute the variance for each principal component. The result is shown in panel (a) of Fig. 9. For PCA, components with variances larger than 1 (shown with a solid black line) should be considered significant. Principal component 1 (PC1) and 2 (PC2) clearly meet this criteria. PC3 hovers just above the line (~ 1.08) and is likely not a significant component.

The resulting PCA is shown in panel (b) of Fig. 9. PC1 accounts for 28.5 per cent of the total variability, while PC2, accounts for 23.8 per cent. NLS1 galaxies are shown as blue points, and BLS1 galaxies are shown as red points. Ellipses mark the parameter space occupied by each distribution. It is apparent that NLS1 galaxies are scattered in the parameter space and several occupy extremes of the parameter space. BLS1 galaxies are more consistent. Of interest is the tight anti-correlation between PC1 and PC2 that exists for BLS1 galaxies, but not for NLS1 galaxies. This behaviour may be highlighting intrinsic differences between NLS1 and BLS1 AGN.

The contributions of each measured parameter to each principal component are shown with dark red arrows. Longer arrows indicate higher contributions to the principal component. To assess the importance of these contributions to each PC, we compute the fractional contribution of each parameter to each of the first three principal components. The results are summarised in Table 4. Parameters that contribute more than the average fractional contribution ($1/7 \approx 0.15$) are considered important contributors to the PC. These values are shown in bold in the table.

Table 4 and panel (b) of Fig. 9 show that PC1 is mostly comprised of contributions from L_x/L_{Edd} , along with weaker contributions from Γ and the iron line strength, Fe/ L_x . As we saw in the correlation analysis, and as discussed in previous works, both Γ and the iron line emission are highly linked to the Eddington ratio. Shemmer et al. (2008) and Brightman et al. (2013), among others, show a strong positive correlation between the Eddington ratio and Γ , which is also seen in this work (see Fig. 6). The X-ray Baldwin effect is also known to produce an anti-correlation between the accretion rate and the equivalent width of the Fe K α line

(e.g. Bianchi et al. 2007), which is seen also in our sample. In the PCA, the correlation between L_x/L_{Edd} and Γ is indicated as both components contribution to PC1 in a correlated manner, while the anti-correlation between iron line strength and L_x/L_{Edd} is shown through the two components having opposite contributions to PC1 (L_x/L_{Edd} and Fe/ L_x point in opposite directions in panel (b) of Fig. 9). It is therefore likely that PC1 is primarily due to variations in L_x/L_{Edd} within the sample.

Examining PC2, we see significant contributions from two components: the soft and hard excess strengths, SE and HE. These both contribute in the same way to PC2, as both arrows point in the same direction in Fig. 9. This is of interest, as the KS test analysis presented in Section 4.4 indicated that the distributions of soft excess and hard excess strengths between NLS1 and BLS1 galaxies were different at the > 99.99 per cent and > 99 per cent levels, respectively, with NLS1 galaxies showing stronger soft and hard excesses. The correlation analysis also showed that these two parameters are significantly correlated, and that this correlation is driven by the NLS1 sample (where $r = 0.55$), while BLS1 galaxies show little evidence for correlation between these parameters ($r = 0.2$).

Although PC3 is likely not an important contributor to the observed variance, we show the fractional contributions of each parameter to this component in Table 4. PC3 is mostly contributions from kT and L_x , with a weak contribution from Γ . Notably, kT and L_x are the two components which were not important in PC1 or PC2. For this reason, and given that PC3 has a low variance, we do not consider this component in further discussion.

As an additional check, we also compute the PCA separately for the NLS1 and BLS1 samples. For the NLS1 sample, only the first two principal components are significant. PC1 is dominated by contributions from the X-ray Eddington ratio, with weaker contributions from L_x and Γ , while PC2 is dominated by the soft and hard excess strengths. This is largely in agreement with what we observe in the the PCA analysis for the full sample, and matches what we observe in the correlation analysis. For the BLS1 sample, PC1 has significant contributions from L_x/L_{Edd} , L_x , and Fe/ L_x . This is sensible, as all these parameters are highly correlated. However, for PC2, we see strong contributions from the soft excess strength and Γ , while there is no significant contribution from the hard excess. This again suggests that the relationship between the soft and hard excess, as well as the overall sample variance, are not the same between the NLS1 and BLS1 samples. These findings will come into play as we examine the markedly different behaviour of NLS1 and BLS1 galaxies seen in panel (b) of Fig. 9 in Section 6.

6 DISCUSSION

6.1 The *Suzaku* sample

Our analysis of a sample of 22 NLS1 and 47 BLS1 galaxies reveals many interesting results. A key advantage of *Suzaku* is that it provides a simultaneous view of the soft excess, Fe K α line, and hard excess, which is advantageous when searching for correlations between these parameters. It is important to note that *Suzaku* is not a survey mission and therefore, the sample is not complete in terms of flux or volume. However, the NLS1 and BLS1 samples cover a similar range of X-ray luminosities and redshifts, which allows comparisons to be made between the X-ray properties of the two samples. The main results of this analysis are:

- (i) In agreement with previous works, the sample shows that NLS1 galaxies have steeper photon indices (Γ), higher X-ray

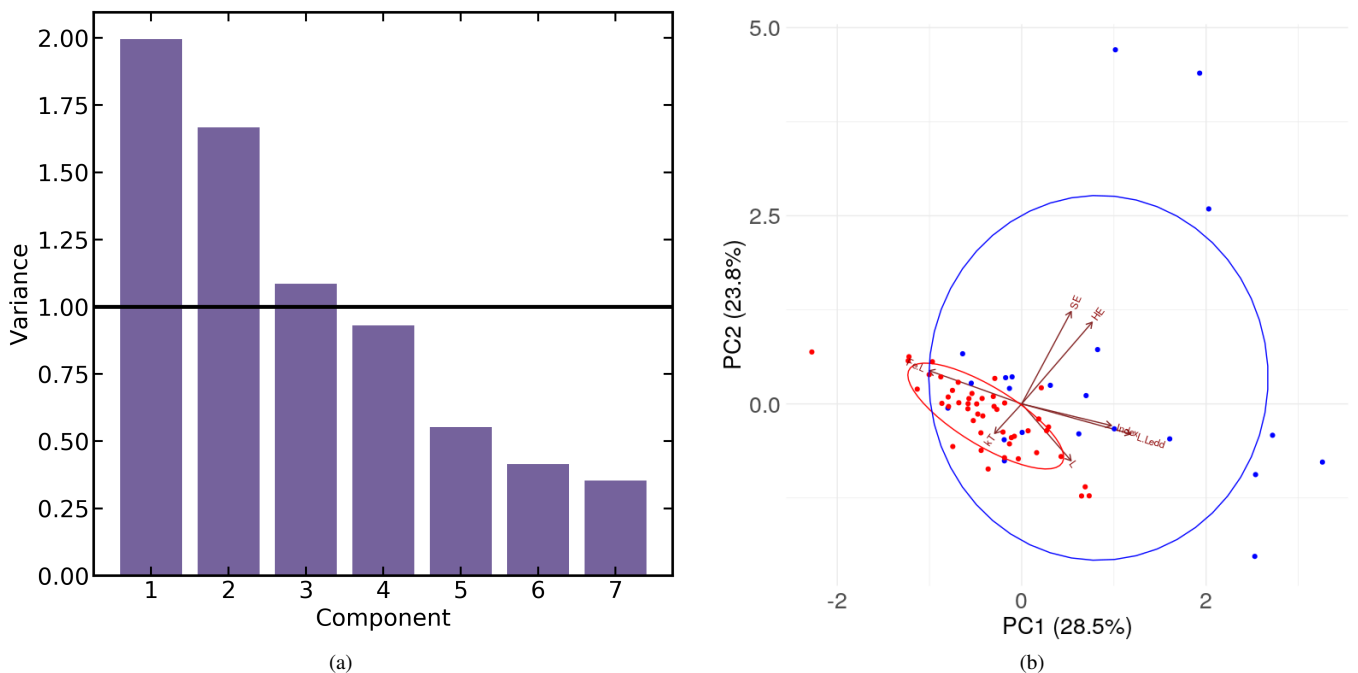


Figure 9. Left: The variance produced by each principal component. A component is considered significant if its variance is greater than 1. PC1 and PC2 are clearly important. The variance in PC3 is only marginally greater than 1. Right: PC2 is plotted as a function of PC1 and the distribution of NLS1s (blue) and BLS1s (red) is shown. The samples overlap, but do appear different. PC2 is largely dominated by the NLS1s. For BLS1s, PC2 appears to be anti-correlated with PC1, but no such correlation is apparent for NLS1s. PC2 is largely composed of contribution for the soft excess (SE) and hard excess (HE) strengths, while significant contributions to PC1 are from the X-ray Eddington ratio (L_x/L_{Edd}), photon index, and Fe/L_x (see Table 4).

Eddington ratios (L_x/L_{Edd}) and stronger soft excesses (SE) than BLS1 galaxies.

- (ii) The luminosity of the narrow Fe $K\alpha$ core is lower on average in NLS1 galaxies. When we divide by the line luminosity by the continuum luminosity (i.e. a proxy for equivalent width) for each AGN (Fe/L_x), this ratio is also weaker for NLS1s.
- (iii) There is a significant correlation between L_x/L_{Edd} and Γ , and a weaker anti-correlation between L_x/L_{Edd} and Fe/L_x (a result of the X-ray Baldwin effect). In the PCA, these three components make up PC1, with the strongest contribution from the X-ray Eddington ratio.
- (iv) NLS1 galaxies, on average, have stronger hard excesses than BLS1 galaxies. For NLS1 galaxies, we also find a significant correlation between the soft and hard excesses, which is not found in the BLS1 galaxies.
- (v) When performing the PCA on the full sample, this SE and HE correlation appears as PC2. When the PCA is repeated for the individual samples, the NLS1s still show the soft and hard excess as PC2. However, for the BLS1s, PC2 shows contributions from the Γ and the soft excess.
- (vi) The PCA shows large overlap between the NLS1 and BLS1 parameter space. However, the behaviours of the two samples are distinct. BLS1 galaxies appear to show an anti-correlation between PC1 and PC2. NLS1 galaxies are more spread out, occupying extreme regions of parameter space.

These results and possible physical interpretations are discussed in more detail in the following sections.

6.2 Iron line properties

When considering the properties of the narrow Fe $K\alpha$ core in our sample, we find some evidence that on average BLS1 galaxies have higher luminosity iron lines than NLS1 galaxies. This is also the case when considering the ratio of iron line luminosity to X-ray luminosity (Fe/L_x ; i.e. a proxy for equivalent width), implying that NLS1 iron lines are also weaker relative to the continuum.

The narrow Fe $K\alpha$ emission likely originates in distant material like the torus or broad line region (e.g. [Nandra et al. 2007](#)). The stronger iron lines in BLS1 galaxies could result from increased contributions from the torus. This could result in high-levels of absorption in the spectra of BLS1s, which is not evident. Using ztbabs as a proxy for overall galaxy absorption, there appears to be little difference in the levels of intrinsic absorption in NLS1s and BLS1s (see panel (b) of Fig. 5).

Previous works show differing interpretations on analyses of absorption in NLS1 galaxies: for example, [Boller et al. \(1996\)](#), find little evidence for large column densities in NLS1 galaxies observed with *ROSAT*. However, some previous interpretations of the properties of NLS1 galaxies (e.g. [Mathur 2000](#); [Williams et al. 2002](#); [Middleton et al. 2007](#)), invoke increased levels of absorption to help explain observed UV and X-ray properties. More consideration to potential explanations of the iron line properties will be given in a future work.

6.3 The soft and hard excesses in Seyfert 1 AGN

Previous works have shown that NLS1 galaxies have steeper and stronger soft excesses than BLS1s (e.g. [Boller et al. 1996](#); [Leighly 1999](#); [Vaughan et al. 1999](#); [Gliozzi & Williams 2020](#); [Ojha et al. 2020](#)), while less is known about the hard excess given the difficulty

in detecting high energy emission. In our sample, NLS1 galaxies have stronger soft and hard excesses (SE and HE) than BLS1 galaxies (see Fig. 5). The re-sampled KS test p-values demonstrate that this distinction can be made even when considering the errors on the parameters. The relationship between these parameters is shown in panel (d) of Fig. 8, where the NLS1s are shown in blue and BLS1s are shown in red. NLS1 galaxies show a significant correlation between SE and HE, which is not seen in the BLS1 sample. The positive correlation seen in the full sample (Fig. 6) is therefore driven mainly by the NLS1s.

The positive correlation between SE and HE in the NLS1 sample may point to a common origin between these two components. In particular, this correlation can be understood and is even predicted from the blurred reflection model (e.g. Ross & Fabian 2005; Vasudevan et al. 2014). In this scenario, photons are emitted isotropically from the corona. While some are observed directly (forming the power law component), others are first reflected off of the innermost accretion disc (e.g. Ross & Fabian 2005). This produces a multitude of fluorescent emission lines at low energies, which are relativistically blurred to form the soft excess. Higher energy photons penetrate further into the disc, where the material becomes more optically thick. These photons then undergo Compton scattering, forming the Compton hump peaking around 20 keV. The ratio of reflected emission to continuum emission is then defined as the reflection fraction, R , which depends primarily upon the geometry of the corona. It is tempting to suggest that the distribution of NLS1 galaxies may be explained by different reflection fractions for each source.

By contrast, the lack of correlation between the soft and hard excesses in the BLS1 galaxies may indicate that the origin of the soft and hard excesses in BLS1s may not necessarily require significant blurred reflection. Boissay et al. (2016) argue that the positive correlation between SE and Γ observed in a BAT sample study, and that is also seen in the BLS1s in this work, cannot be explained with a blurred reflection model. Separate mechanisms may instead be responsible for the production of the soft and hard excesses (e.g. partial covering or soft Comptonisation producing the soft excess, and reflection from neutral material which produces the Compton hump). The narrow range of observed soft excesses in the BLS1 sample is also of interest and worthy of further exploration.

Correlations between these parameters have been studied in previous works. Vasudevan et al. (2014) present a similar positive correlation using data from *XMM-Newton* and the BAT 58 month catalogue. This work uses a ratio of blackbody emission from 0.4 – 3 keV and power law emission from 1.5 – 6 keV to define the soft excess, and the reflection fraction R from the PEXRAV (Magdziarz & Zdziarski 1995) to define the strength of the Compton hump, differing slightly from our analysis. This work also cautions that non-simultaneous observations of the soft and hard energy bands are used, which may affect model parameters. Boissay et al. (2016) use a sample of type 1 AGN observed with *XMM-Newton* and *Swift* BAT and instead find an anti-correlation between the soft excess strength and the reflection fraction. This trend is also found when considering a sample of only 10 NLS1 galaxies. However, this work again uses different definitions for the soft excess and R , complicating a direct comparison of results.

Vasudevan et al. (2014) and Boissay et al. (2016) also present theoretical relationships between the hard excess (R) and soft excess based on blurred reflection simulations. In both works, these simulations show a positive correlation between the soft excess and R , akin to the one seen in our NLS1 sample. In particular, Vasudevan et al. (2014) show that blurred reflection simulations can result

in extremely strong soft excesses like the ones observed in some NLS1s in our sample. This lends further evidence that the soft and hard excesses in NLS1s may be produced through blurred reflection. By contrast, Vasudevan et al. (2014) perform ionised absorption simulations and find no evidence for a correlation between the soft excess and R , similar to what we observe in our BLS1 sample. It is therefore plausible to suggest that ionised partial covering (e.g. Tanaka et al. 2004; Chevallier et al. 2006; Iso et al. 2016), or warm Comptonisation (e.g. Petrucci et al. 2018; Ballantyne 2020), may be responsible for shaping some of the soft excesses observed in BLS1s.

The results of the PCA further support the distinct origins for the soft and hard excesses in the two samples. First, we note that the PCA performed on the full sample and on the NLS1s and BLS1s consistently reveals the X-ray Eddington ratio, L_x/L_{Edd} , as the main contributor to PC1. However, the contributors to PC2 change depending on which sample is used. For the full sample, PC2 is dominated by changes in the soft and hard excesses. The SE and HE also form PC2 for the NLS1 sample, suggesting that these galaxies drive PC2 for the full sample. When only the BLS1 galaxies are used, PC2 instead becomes dominated by a combination of the soft excess and Γ . The PC2 results therefore appear to match the correlation analysis, and may demand a different origin for the soft excess in the two samples.

Another feature highlighting the differences between the two samples is the distribution of BLS1 galaxies in panel (b) of Fig. 9. The BLS1 galaxies show a strong anti-correlation between PC1 and PC2, while no such correlation is seen in the NLS1 sample. This may be explained as a mathematical artefact of the PCA due to the large variance within the NLS1 sample. Such mathematical artefacts have been previously observed in PCA analysis; Gallant et al. (2018) show that for spectral PCAs performed on a sample of blazars, PC3 sometimes appears as a distinctive bowed feature. Based on simulation work, this PC shape does not appear to represent a physical process, but rather a mathematical artefact resulting from the first two PCs. The anti-correlation observed here may have a similar origin. When the PCA is performed separately on the NLS1 and BLS1 samples, no such anti-correlation exists.

If this is indeed the case, this artefact may appear due to the much larger variance within the NLS1 sample. Several NLS1 sources have extreme soft excesses (1H0707-495, PG1404+226, RE J1034+396), and others are radio loud and have high X-ray Eddington ratios (PKS 0558-504, RX J0134.2-4258, RX J1633.3+4718). These sources all appear as outliers in panel (b) of Fig. 9. This again highlights the extreme behaviour of the NLS1 sample and further suggests intrinsic spectral differences between the two samples, and in particular, in the measured soft and hard excesses.

7 CONCLUSIONS

In this work, we present a sample of Seyfert 1 galaxies observed with *Suzaku*. We select all NLS1 and BLS1 galaxies with redshifts < 0.5 and low host-galaxy column densities ($< 10^{22} \text{ cm}^{-2}$) observed with *Suzaku*. This results in a sample of 69 AGN, of which 22 are NLS1s and 47 are BLS1s. These selection criteria allow for proper characterisation of the soft excess, often observed below ~ 2 keV. The sample covers a similar range of redshifts and X-ray luminosities for both classes and is thus ideal for probing differences between the X-ray emission in NLS1 and BLS1 galaxies.

In this work, we have focussed on measuring and comparing the broad band X-ray spectral properties of NLS1 and BLS1 galaxies using a toy model, which confirmed many previous results as well as presenting new findings on the soft and hard excesses. The acquired sample is suitable for the analysis of many additional properties of type-1 AGN, including further spectral and variability analysis.

This work has shown that the soft excess, and the relationship between the soft and hard excesses, are important characteristics in distinguishing the X-ray properties of Seyfert 1 galaxies. The work highlights the importance of simultaneous broadband X-ray spectroscopy to uncover the nature of the soft and hard excess in Seyfert 1 galaxies.

ACKNOWLEDGEMENTS

We thank the referee for their helpful comments and suggestions which improved this manuscript. We would also like to thank Adam Gonzalez for helpful discussions. This research has made use of data obtained from the *Suzaku* satellite, a collaborative mission between the space agencies of Japan (JAXA) and the USA (NASA). The authors acknowledge the support of the Natural Sciences and Engineering Research Council of Canada (NSERC). LCG acknowledges financial support from the Canadian Space Agency (CSA).

DATA AVAILABILITY

The data used in this work are publicly available in the *Suzaku* DARTS archive (<https://darts.isas.jaxa.jp/astro/suzaku/data/>).

REFERENCES

- Alston W. N., et al., 2019, *MNRAS*, **482**, 2088
- Arnaud K. A., 1996, in Jacoby G. H., Barnes J., eds, *Astronomical Society of the Pacific Conference Series Vol. 101, Astronomical Data Analysis Software and Systems V*. p. 17
- Ballantyne D. R., 2005, *MNRAS*, **362**, 1183
- Ballantyne D. R., 2020, *MNRAS*, **491**, 3553
- Ballantyne D. R., Ross R. R., Fabian A. C., 2001, *MNRAS*, **327**, 10
- Ballo L., Braitto V., Reeves J. N., Sambruna R. M., Tombesi F., 2011, *MNRAS*, **418**, 2367
- Barth A. J., et al., 2011, *ApJ*, **732**, 121
- Bentz M. C., Katz S., 2015, *PASP*, **127**, 67
- Bian W., Zhao Y., 2003, *MNRAS*, **343**, 164
- Bianchi S., Guainazzi M., Matt G., Fonseca Bonilla N., 2007, *A&A*, **467**, L19
- Boissay R., Ricci C., Paltani S., 2016, *A&A*, **588**, A70
- Boller T., Brandt W. N., Fink H., 1996, *AAP*, **305**, 53
- Boller T., et al., 2002, *MNRAS*, **329**, L1
- Boroson T. A., Green R. F., 1992, *ApJs*, **80**, 109
- Brandt W. N., Mathur S., Elvis M., 1997, *MNRAS*, **285**, L25
- Brightman M., et al., 2013, *MNRAS*, **433**, 2485
- Buhariwalla M. Z., Waddell S. G. H., Gallo L. C., Grupe D., Komossa S., 2020, arXiv e-prints, p. arXiv:2008.08027
- Cash W., 1979, *ApJ*, **228**, 939
- Chevallier L., Collin S., Dumont A. M., Czerny B., Mouchet M., Gonçalves A. C., Goosmann R., 2006, *A&A*, **449**, 493
- Crummy J., Fabian A. C., Gallo L., Ross R. R., 2006, *MNRAS*, **365**, 1067
- Czerny B., et al., 2016, *A&A*, **594**, A102
- Done C., Davis S. W., Jin C., Blaes O., Ward M., 2012, *MNRAS*, **420**, 1848
- Du P., et al., 2018, *ApJ*, **869**, 142
- Fabian A. C., Rees M. J., Stella L., White N. E., 1989, *MNRAS*, **238**, 729
- Fabian A. C., et al., 2012, *MNRAS*, **419**, 116
- Fukazawa Y., et al., 2009, *PASJ*, **61**, S17
- Fukazawa Y., et al., 2011, *ApJ*, **727**, 19
- Fukazawa Y., Furui S., Hayashi K., Ohno M., Hiragi K., Noda H., 2016, *ApJ*, **821**, 15
- Gallant D., Gallo L. C., Parker M. L., 2018, *MNRAS*, **480**, 1999
- Gallo L. C., 2006, *MNRAS*, **368**, 479
- Gallo L., 2018, in *Revisiting Narrow-Line Seyfert 1 Galaxies and their Place in the Universe*. p. 34 (arXiv:1807.09838)
- Gallo L. C., Boller T., Brandt W. N., Fabian A. C., Grupe D., 2004, *MNRAS*, **352**, 744
- Gallo L. C., et al., 2019, *MNRAS*, **484**, 4287
- Gierliński M., Done C., 2004, *MNRAS*, **349**, L7
- Gliozzi M., Williams J. K., 2020, *MNRAS*, **491**, 532
- Gliozzi M., Papadakis I. E., Brinkmann W. P., 2007, *ApJ*, **656**, 691
- González-Martín O., Vaughan S., 2012, *A&A*, **544**, A80
- Goodrich R. W., 1989, *ApJ*, **342**, 224
- Grupe D., 1996, PhD thesis, -
- Grupe D., 2004, *ApJ*, **127**, 1799
- Grupe D., Leighly K. M., Thomas H. C., Laurent-Muehleisen S. A., 2000, *A&A*, **356**, 11
- Grupe D., Mathur S., Komossa S., 2004, *ApJ*, **127**, 3161
- Grupe D., Komossa S., Leighly K. M., 2010, in *Maraschi L., Ghisellini G., Della Ceca R., Tavecchio F., eds, Astronomical Society of the Pacific Conference Series Vol. 427, Accretion and Ejection in AGN: a Global View*. p. 86
- Haardt F., Maraschi L., 1991, *ApJ*, **380**, L51
- Haardt F., Maraschi L., 1993, *ApJ*, **413**, 507
- Ishida M., et al., 2011, *PASJ*, **63**, S657
- Iso N., Ebisawa K., Sameshima H., Mizumoto M., Miyakawa T., Inoue H., Yamasaki H., 2016, *PASJ*, **68**, S27
- Iwasawa K., Taniguchi Y., 1993, *ApJ*, **413**, L15
- Kaastra J. S., Bleeker J. A. M., 2016, *AAP*, **587**, A151
- Kettula K., Nevalainen J., Miller E. D., 2013, *A&A*, **552**, A47
- Koss M., et al., 2017, *ApJ*, **850**, 74
- La Mura G., Ciroi S., Cracco V., Ilie D., Popovic L., Rafanelli P., 2011, in *Narrow-Line Seyfert 1 Galaxies and their Place in the Universe*. p. 56 (arXiv:1106.2454)
- Landt H., et al., 2017, *MNRAS*, **464**, 2565
- Leighly K. M., 1999, *ApJs*, **125**, 317
- Liebmann A. C., Fabian A. C., Tsuruta S., Haba Y., Kunieda H., 2018, *ApJ*, **868**, 11
- Lusso E., et al., 2010, *A&A*, **512**, A34
- Lusso E., et al., 2012, *MNRAS*, **425**, 623
- Magdziarz P., Zdziarski A. A., 1995, *MNRAS*, **273**, 837
- Magdziarz P., Blaes O. M., Zdziarski A. A., Johnson W. N., Smith D. A., 1998, *MNRAS*, **301**, 179
- Malizia A., et al., 2008, *MNRAS*, **389**, 1360
- Mallick L., Dewangan G. C., 2018, *ApJ*, **863**, 178
- Mantovani G., Nandra K., Ponti G., 2016, *MNRAS*, **458**, 4198
- Mateos S., et al., 2010, *A&A*, **510**, A35
- Mathur S., 2000, *MNRAS*, **314**, L17
- Mathur S., et al., 2018, *ApJ*, **866**, 123
- Middleton M., Done C., Gierliński M., 2007, *MNRAS*, **381**, 1426
- Miniutti G., Piconcelli E., Bianchi S., Vignali C., Bozzo E., 2010, *MNRAS*, **401**, 1315
- Miniutti G., et al., 2014, *MNRAS*, **437**, 1776
- Mitsuda K., et al., 2007, *PASJ*, **59**, S1
- Miyaji T., Ishisaki Y., Ueda Y., Ogasaka Y., Awaki H., Hayashida K., 2003, *PASJ*, **55**, L11
- Miyazawa T., Haba Y., Kunieda H., 2009, *PASJ*, **61**, 1331
- Nandra K., Pounds K. A., 1994, *MNRAS*, **268**, 405
- Nandra K., O'Neill P. M., George I. M., Reeves J. N., 2007, *MNRAS*, **382**, 194
- Nelson C. H., Whittle M., 1995, *ApJS*, **99**, 67
- Nikolačuk M., Czerny B., Gurynowicz P., 2009, *MNRAS*, **394**, 2141
- Noda H., Done C., 2018, *MNRAS*, **480**, 3898

- Noda H., Makishima K., Nakazawa K., Uchiyama H., Yamada S., Sakurai S., 2013, *PASJ*, 65, 4
- Nowak M. A., et al., 2011, *ApJ*, 728, 13
- Ojha V., Chand H., Dewangan G. C., Rakshit S., 2020, arXiv e-prints, p. arXiv:2005.08352
- Osterbrock D. E., Pogge R. W., 1985, *ApJ*, 297, 166
- Paliya V. S., Sahayanathan S., Parker M. L., Fabian A. C., Stalin C. S., Anjum A., Pandey S. B., 2014, *ApJ*, 789, 143
- Petrucchi P. O., Ursini F., De Rosa A., Bianchi S., Cappi M., Matt G., Dadina M., Malzac J., 2018, *A&A*, 611, A59
- Ponti G., Papadakis I., Bianchi S., Guainazzi M., Matt G., Uttley P., Bonilla N. F., 2012, *A&A*, 542, A83
- Porquet D., Reeves J. N., O'Brien P., Brinkmann W., 2004, *AAP*, 422, 85
- Pounds K. A., Nandra K., Stewart G. C., George I. M., Fabian A. C., 1990, *Nature*, 344, 132
- Pounds K. A., Done C., Osborne J. P., 1995, *MNRAS*, 277, L5
- Reeves J. N., Turner M. J. L., 2000, *MNRAS*, 316, 234
- Reeves J. N., et al., 2006, *Astronomische Nachrichten*, 327, 1079
- Rivers E., Markowitz A., Rothschild R., 2011, *ApJ*, 732, 36
- Ross R. R., Fabian A. C., 2005, *MNRAS*, 358, 211
- Schmid H. M., Appenzeller I., Burch U., 2003, *A&A*, 404, 505
- Shemmer O., Brandt W. N., Netzer H., Maiolino R., Kaspi S., 2008, *ApJ*, 682, 81
- Soldi S., et al., 2014, *AAP*, 563, A57
- Tanaka Y., Boller T., Gallo L., Keil R., Ueda Y., 2004, *PASJ*, 56, L9
- Tawa N., et al., 2008, *PASJ*, 60, S11
- Tortosa A., 2017, in Ness J.-U., Migliari S., eds, *The X-ray Universe 2017*. p. 225
- Tripathi S., Waddell S. G. H., Gallo L. C., Welsh W. F., Chiang C. Y., 2019, *MNRAS*, 488, 4831
- Vasudevan R. V., Fabian A. C., 2007, *MNRAS*, 381, 1235
- Vasudevan R. V., Fabian A. C., 2009, *MNRAS*, 392, 1124
- Vasudevan R. V., Mushotzky R. F., Winter L. M., Fabian A. C., 2009, *MNRAS*, 399, 1553
- Vasudevan R. V., Mushotzky R. F., Reynolds C. S., Fabian A. C., Lohfink A. M., Zoghbi A., Gallo L. C., Walton D., 2014, *ApJ*, 785, 30
- Vaughan S., Reeves J., Warwick R., Edelson R., 1999, *MNRAS*, 309, 113
- Vestergaard M., 2002, *ApJ*, 571, 733
- Walter R., Fink H. H., 1993, *A&A*, 274, 105
- Walton D. J., Nardini E., Fabian A. C., Gallo L. C., Reis R. C., 2013a, *MNRAS*, 428, 2901
- Walton D. J., et al., 2013b, *ApJ*, 777, L23
- Wang T., Lu Y., 2001, *A&A*, 377, 52
- Wang T., Brinkmann W., Bergeron J., 1996, *A&A*, 309, 81
- Wang J., Mao Y. F., Wei J. Y., 2009, *AJ*, 137, 3388
- Wilkins D. R., Gallo L. C., Grupe D., Bonson K., Komossa S., Fabian A. C., 2015, *MNRAS*, 454, 4440
- Williams R. J., Pogge R. W., Mathur S., 2002, *AJ*, 124, 3042
- Willingale R., Starling R. L. C., Beardmore A. P., Tanvir N. R., O'Brien P. T., 2013, *MNRAS*, 431, 394
- Wilms J., Allen A., McCray R., 2000, *ApJ*, 542, 914
- Winter L. M., Lewis K. T., Koss M., Veilleux S., Keeney B., Mushotzky R. F., 2010, *ApJ*, 710, 503
- Woo J.-H., Urry C. M., 2002, *ApJ*, 579, 530
- Woo J.-H., Kim J. H., Imanishi M., Park D., 2012, *AJ*, 143, 49
- You B., Cao X.-W., Yuan Y.-F., 2016, *Research in Astronomy and Astrophysics*, 16, 55
- Yuan W., Liu B. F., Zhou H., Wang T. G., 2010, *ApJ*, 723, 508

APPENDIX A: FULL SAMPLE SPECTRA

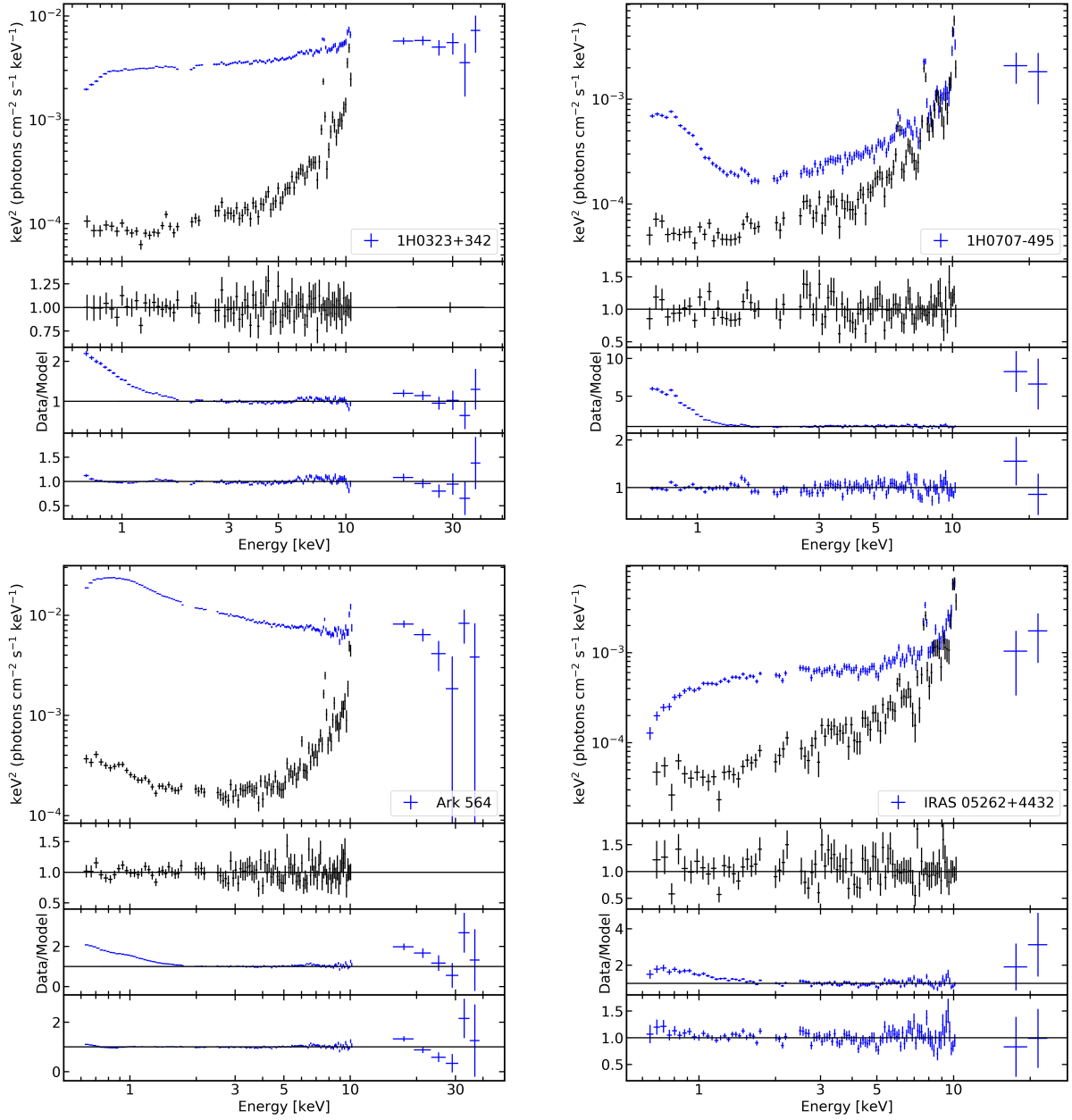


Figure A1. Modelling procedures shown for each AGN in the sample. NLS1 sources are shown in blue, and BLS1s are shown in red. The top panel shows the source+background XIS and PIN data (blue/red) and background (black) unfolded against a power law with $\Gamma = 0$. Object names are given in the bottom right corner. The second panel shows the residuals (data/model) for the background spectrum. The third panel shows the residuals for a power law fit from 2 – 4 and 7 – 10 keV, extrapolated to the full energy range. The last panel shows the residuals for the broad band model. PIN data have been rebinned for clarity.

This paper has been typeset from a $\text{\TeX}/\text{\LaTeX}$ file prepared by the author.

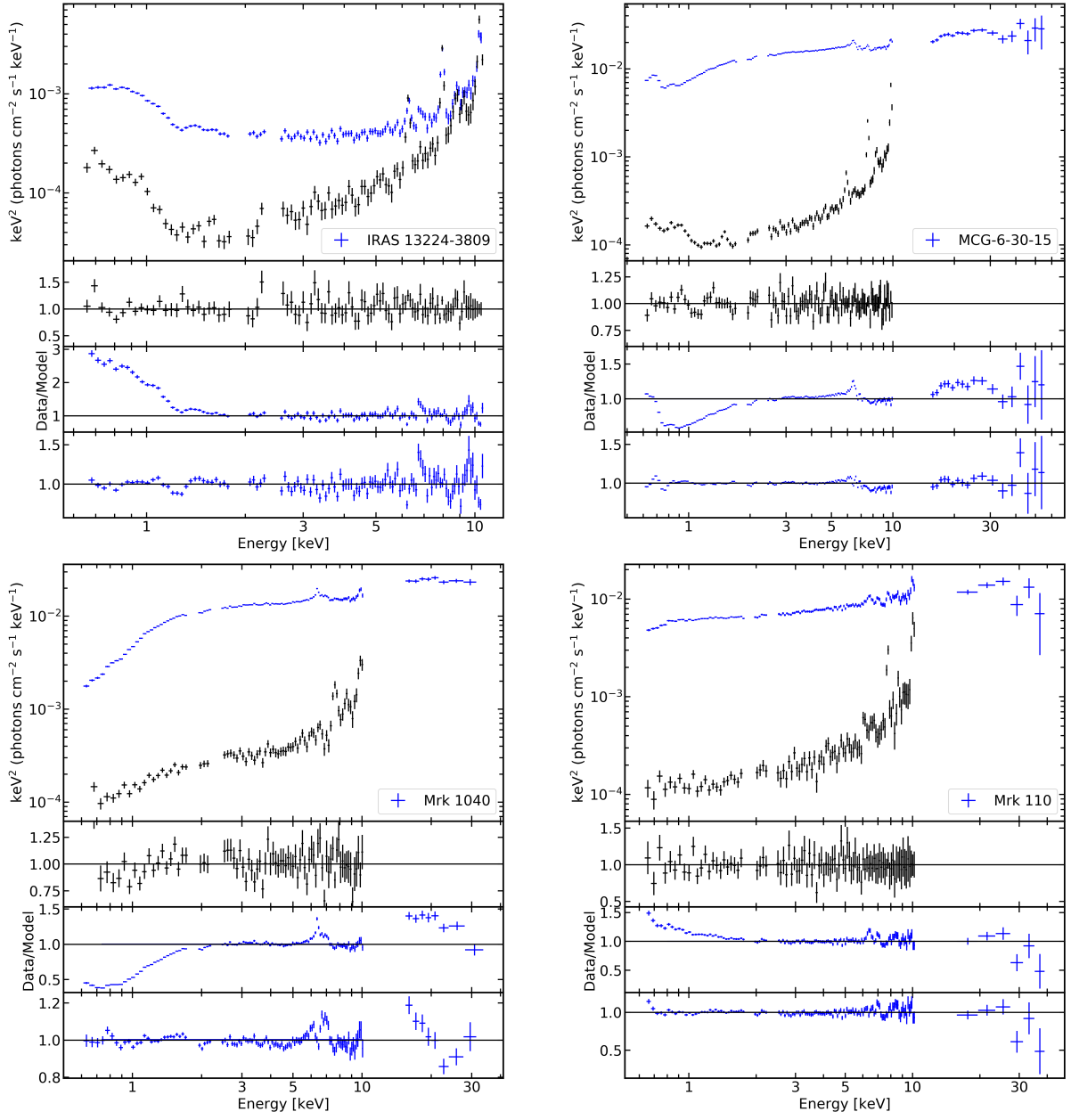


Figure A1. continued

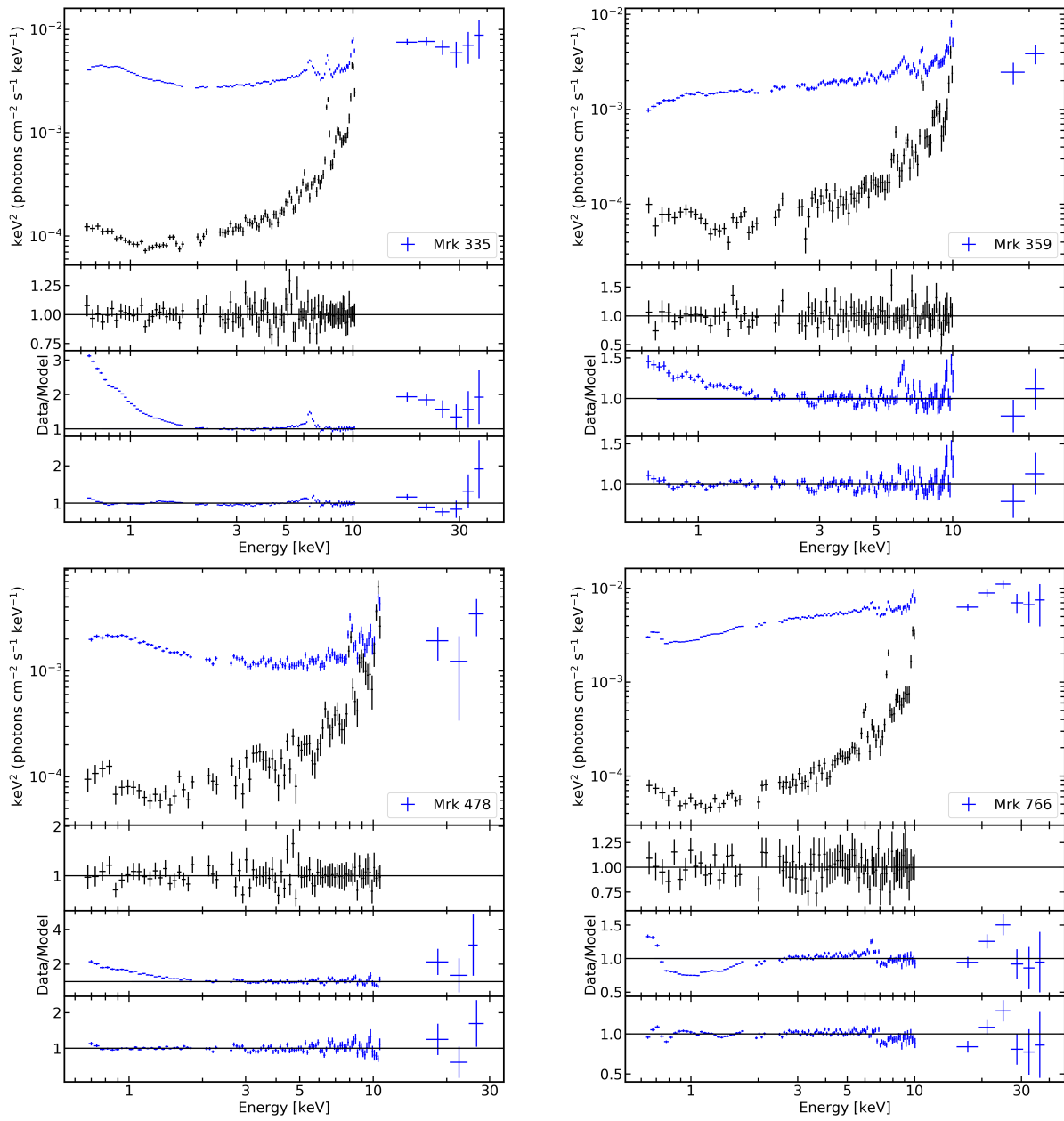


Figure A1. continued

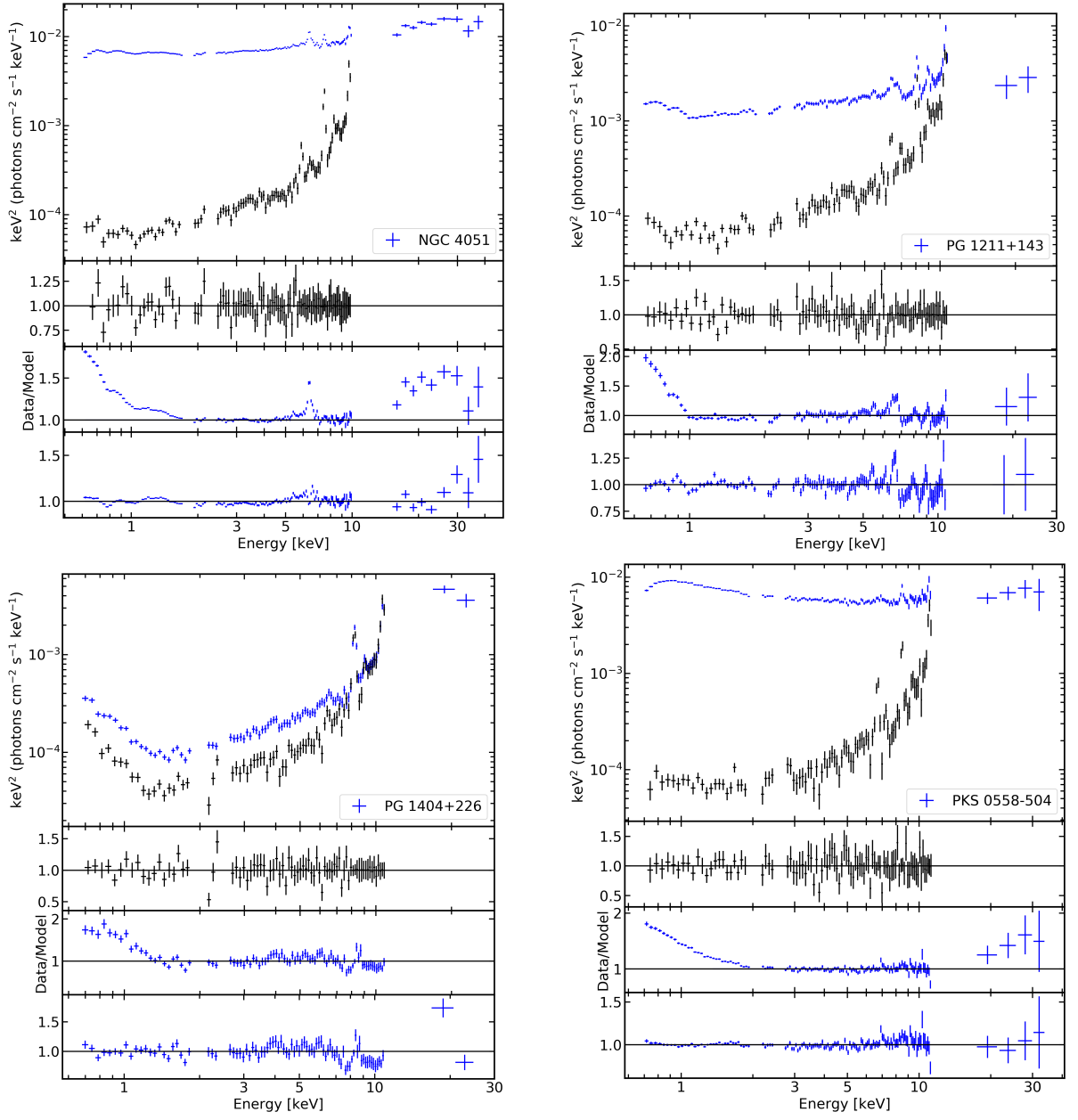


Figure A1. continued

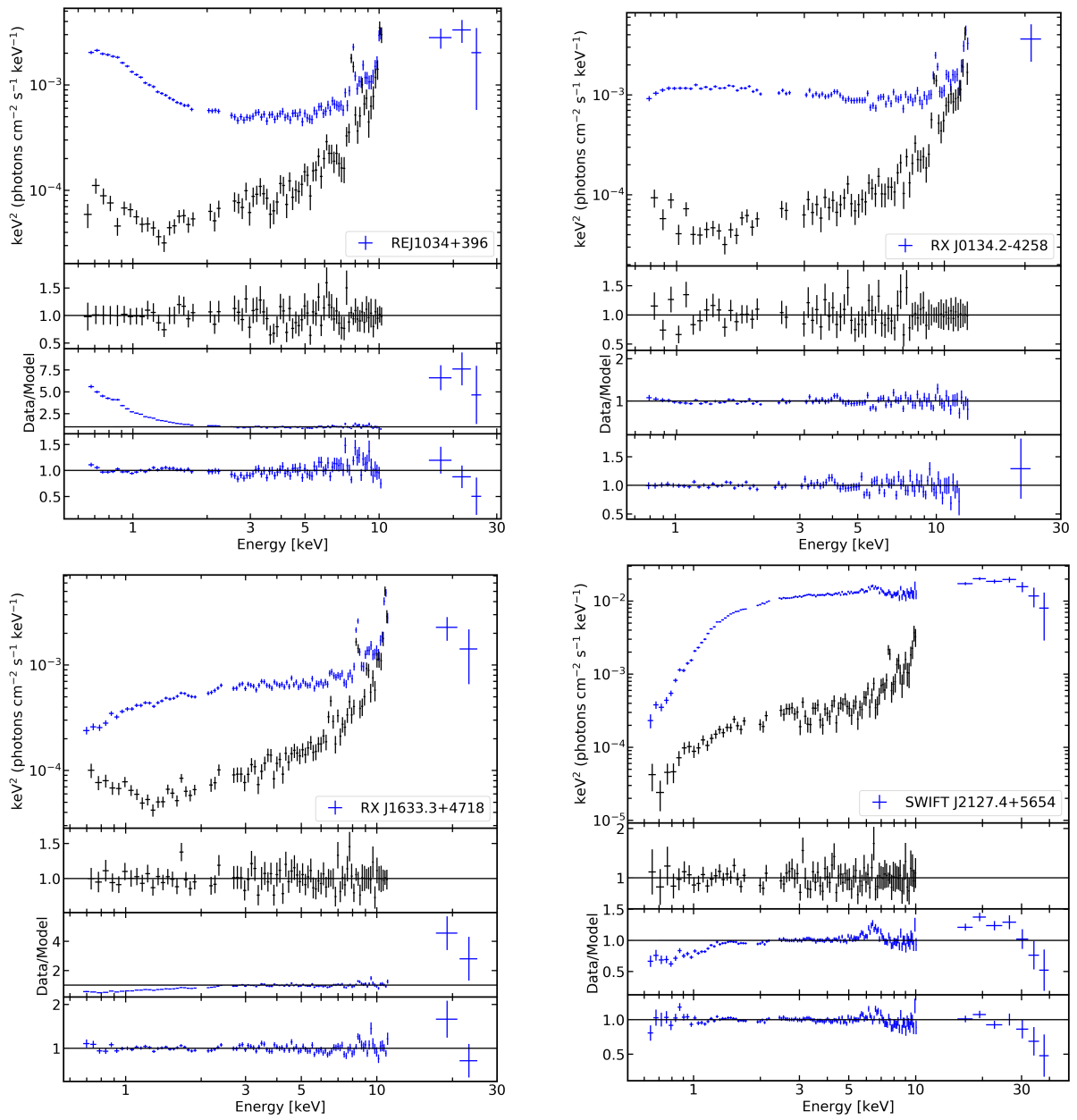


Figure A1. continued

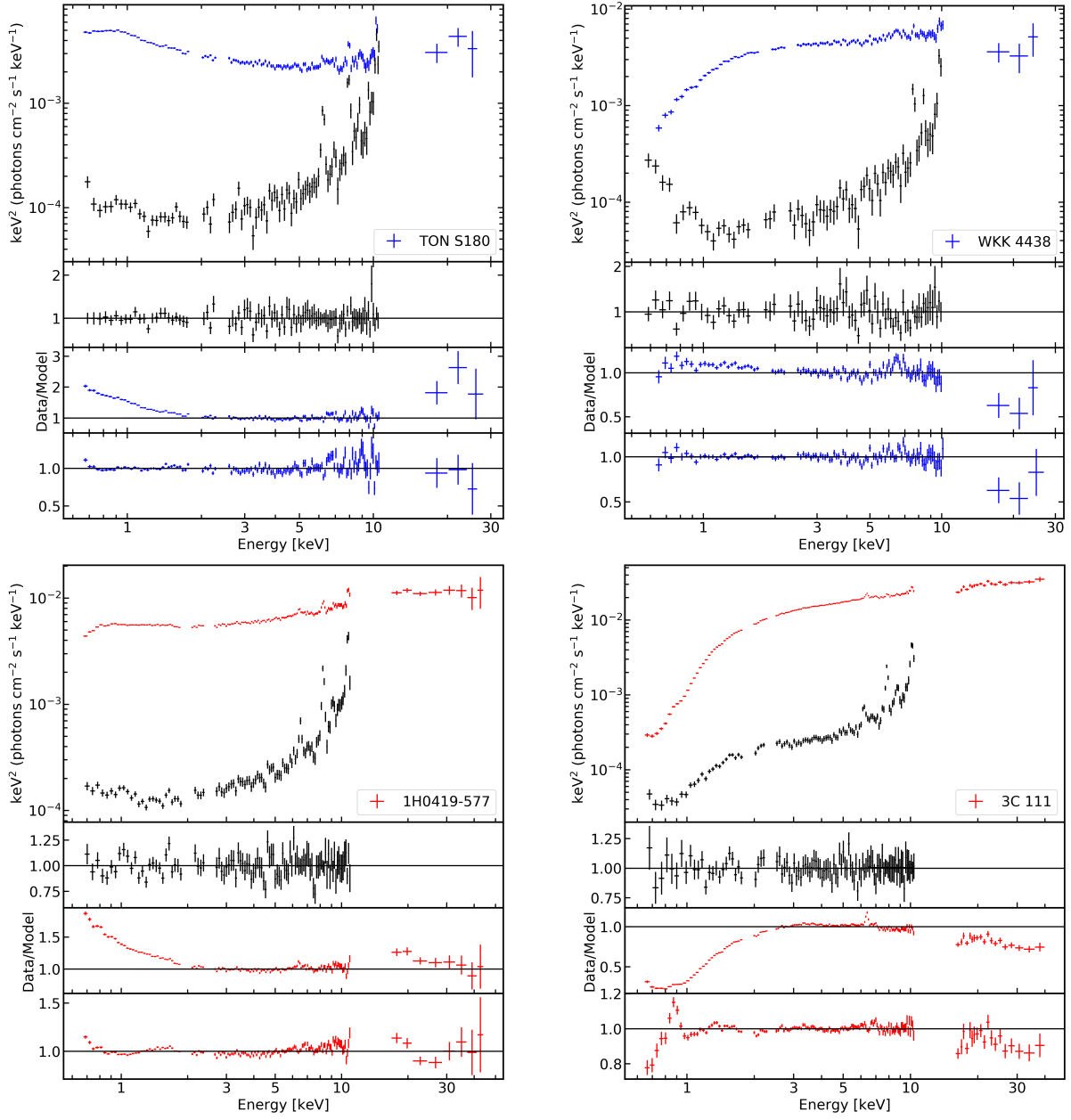


Figure A1. continued

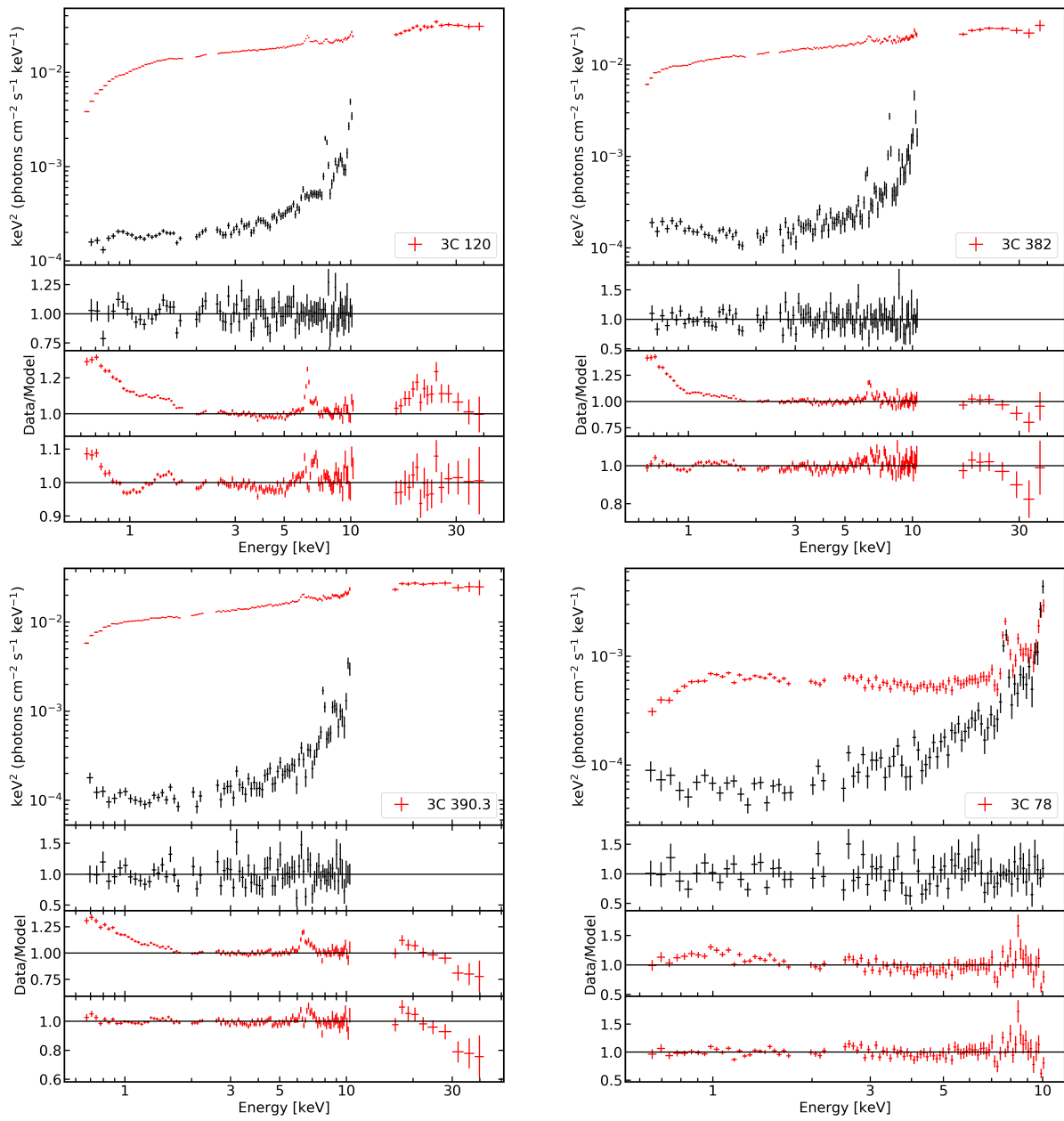


Figure A1. continued

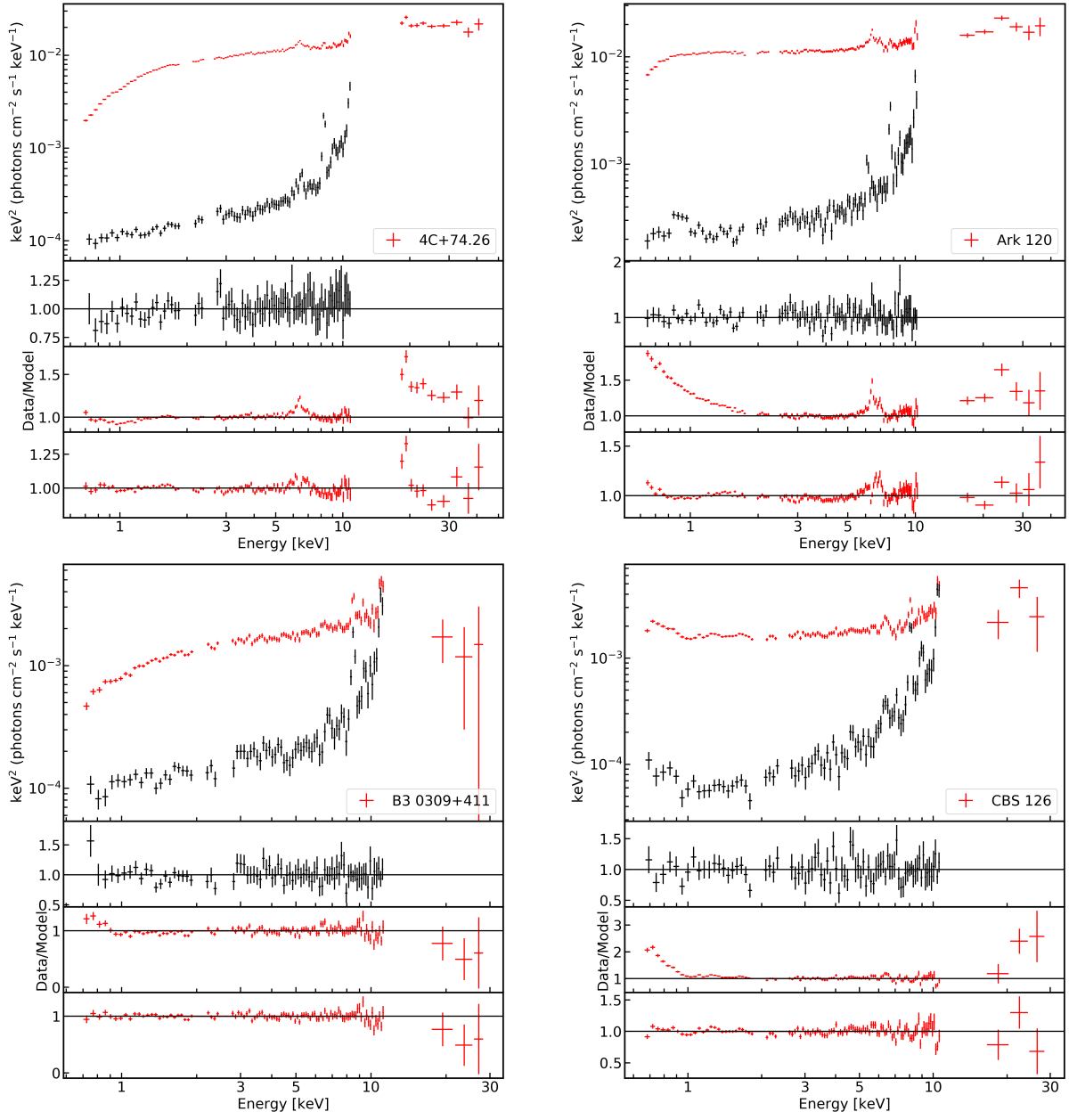


Figure A1. continued

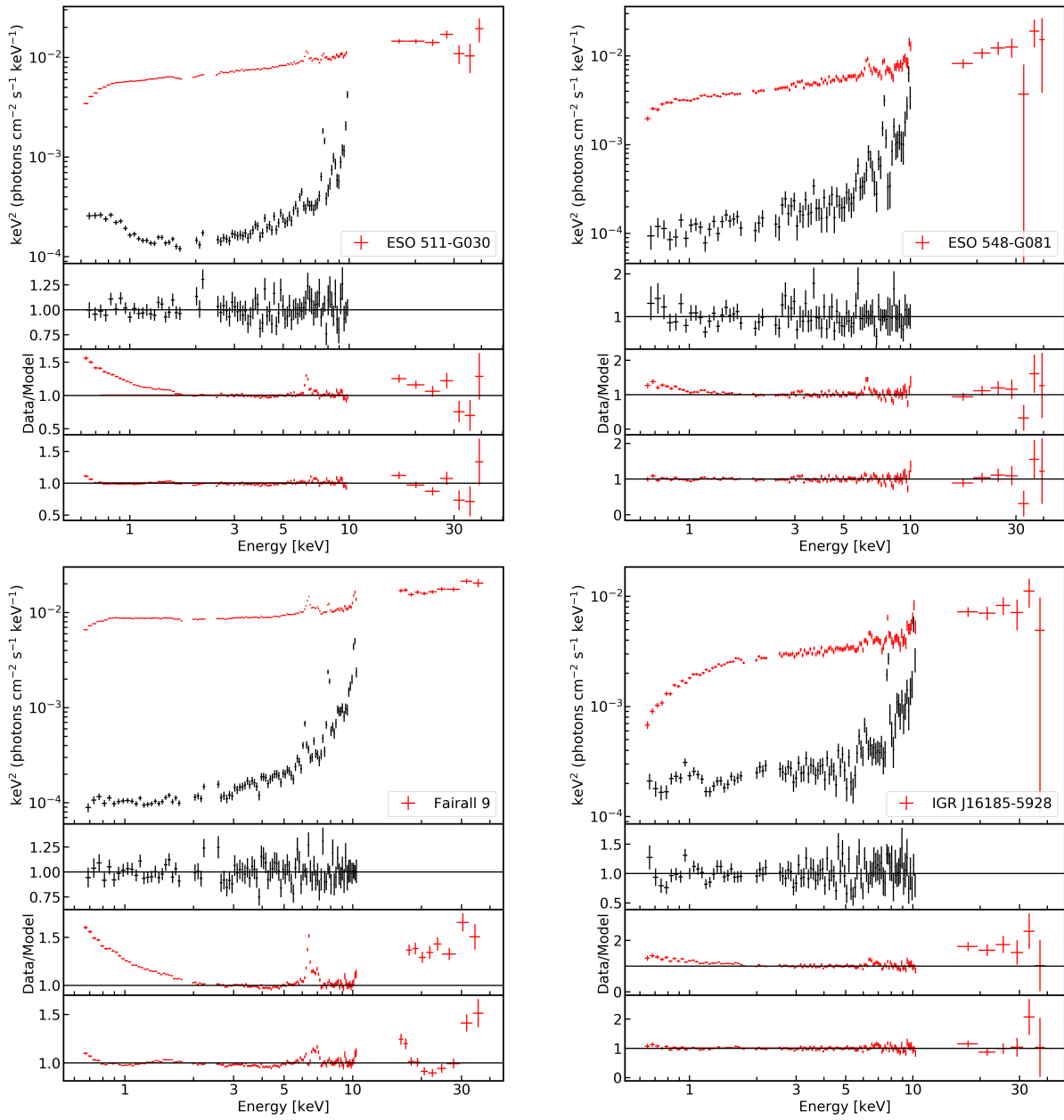


Figure A2. continued

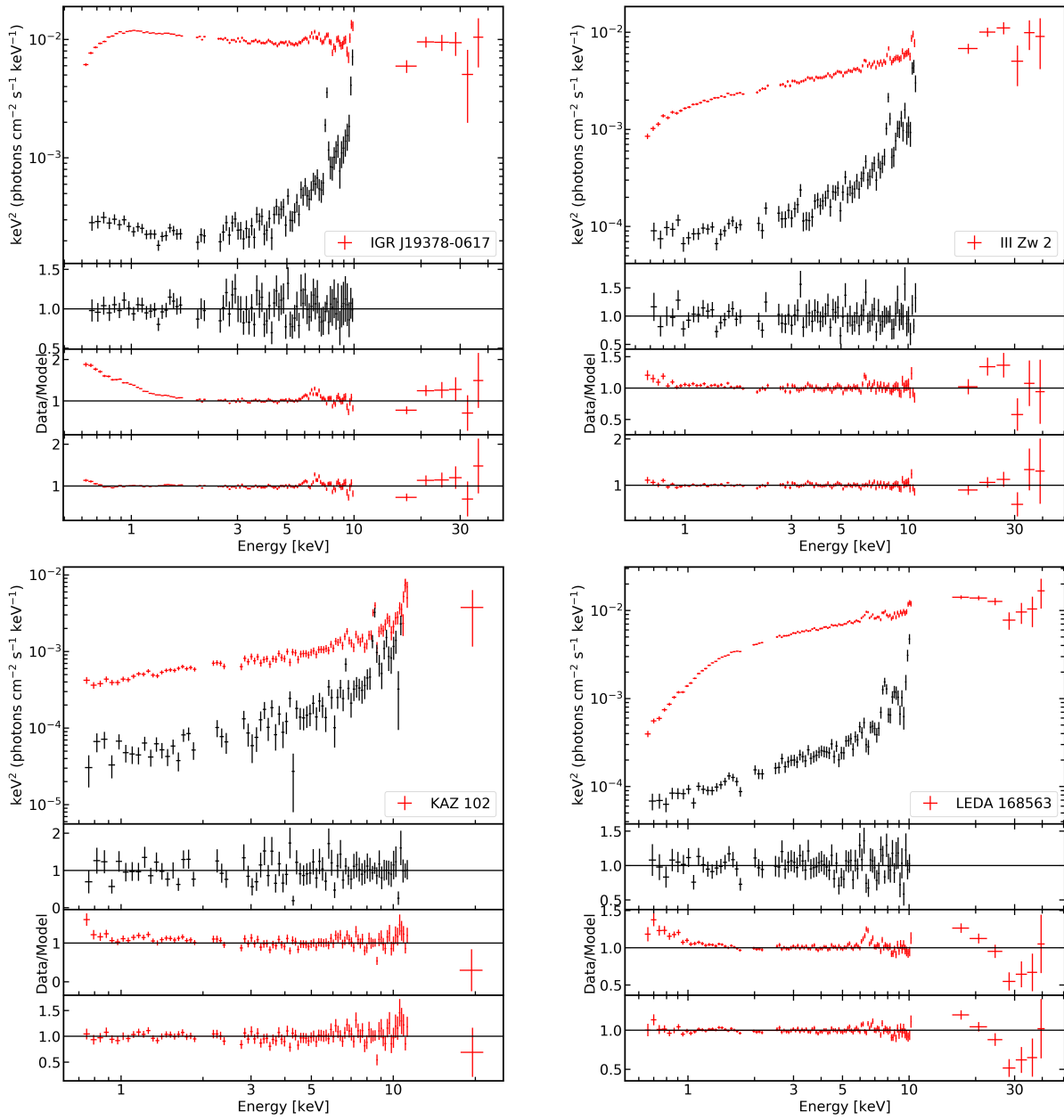


Figure A1. continued

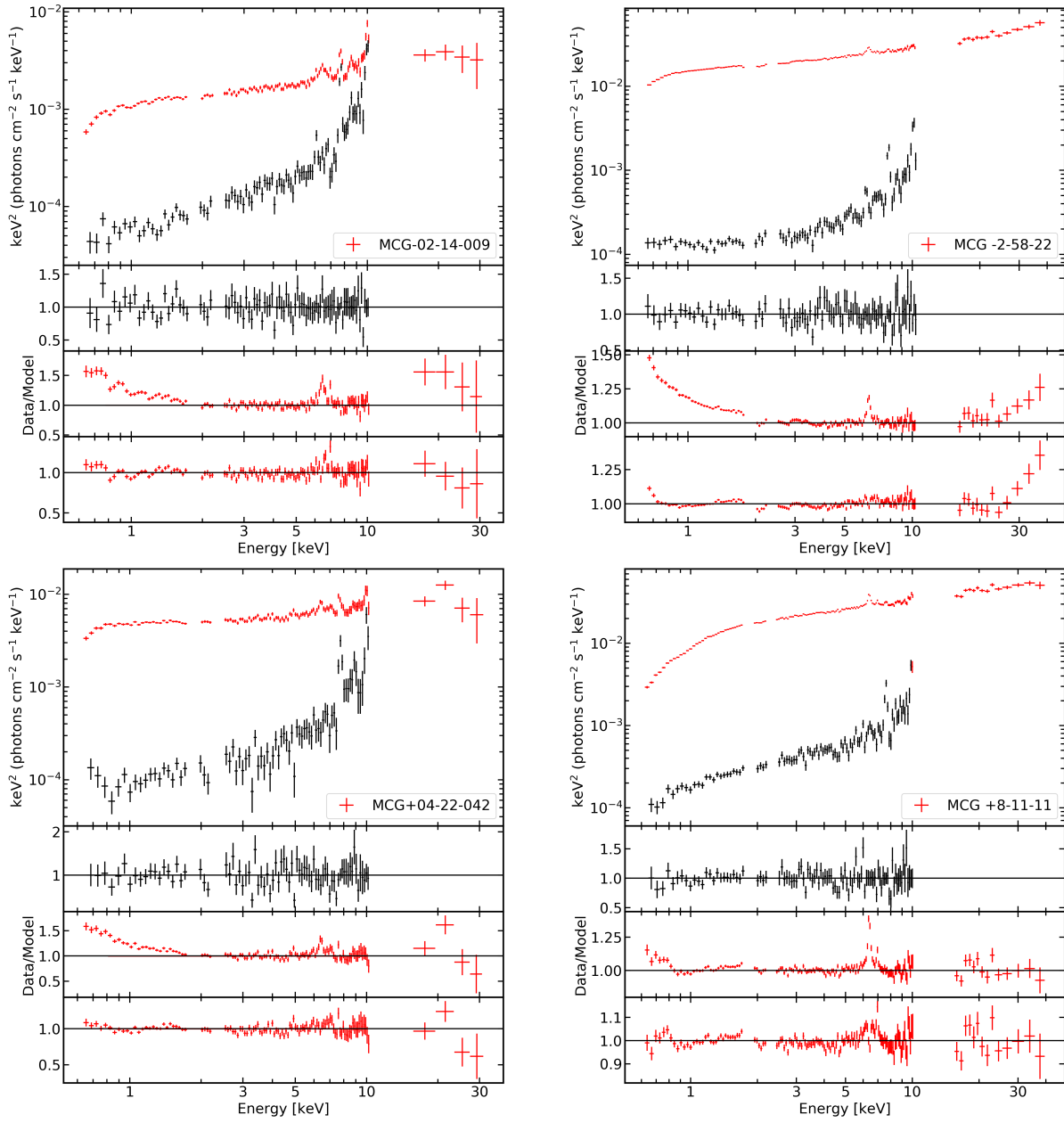


Figure A1. continued

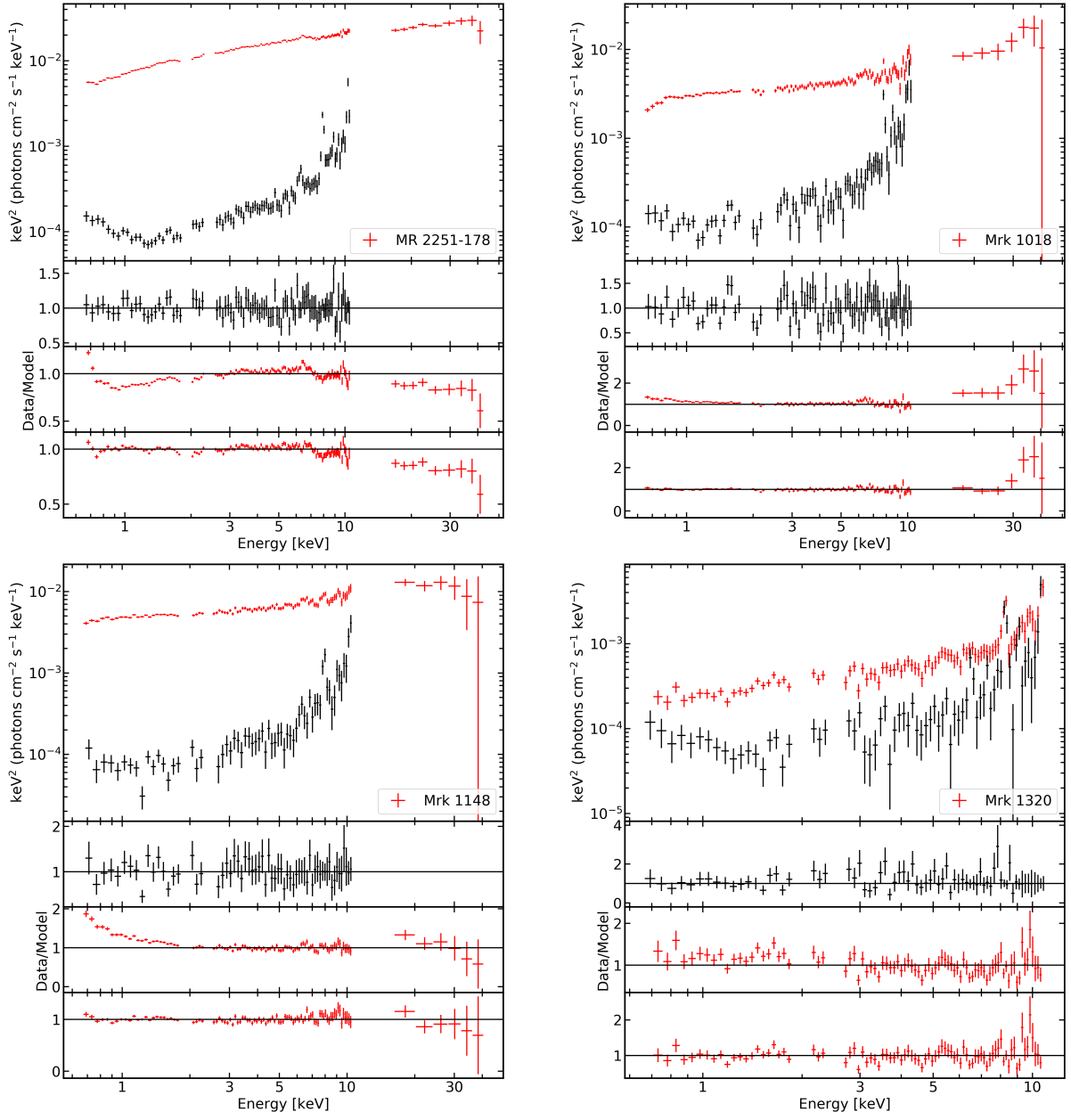


Figure A1. continued

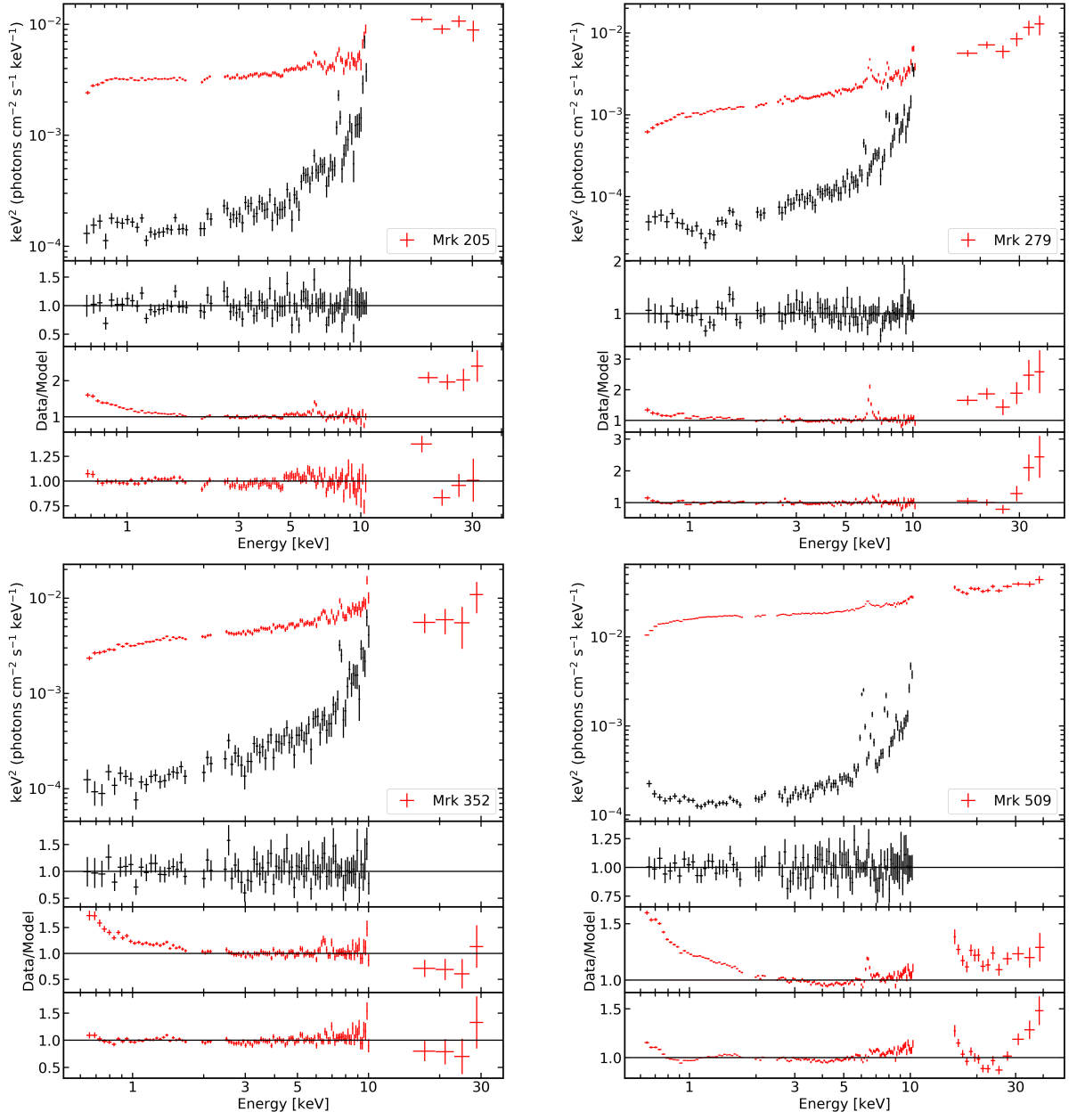


Figure A1. continued

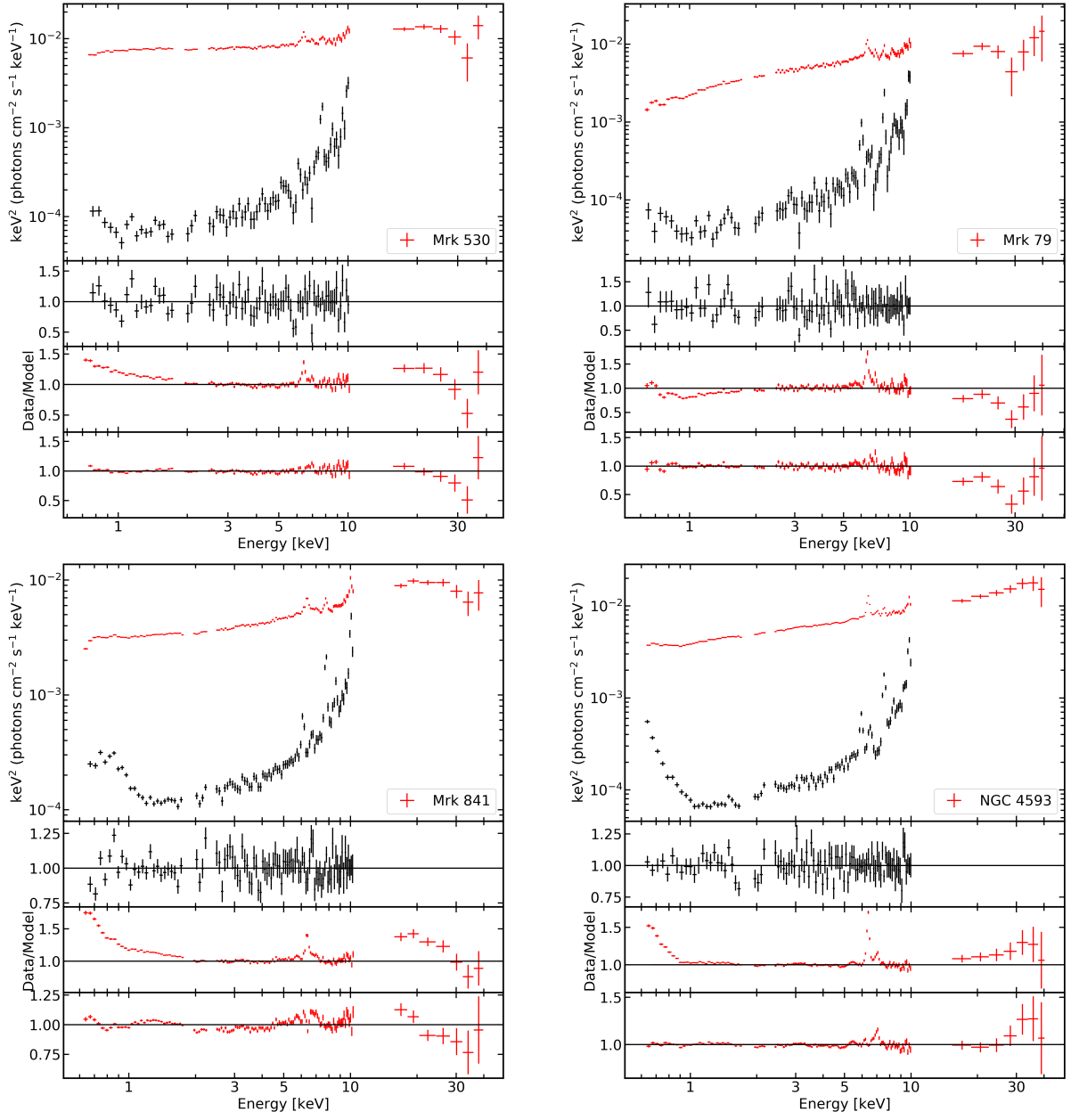


Figure A1. continued

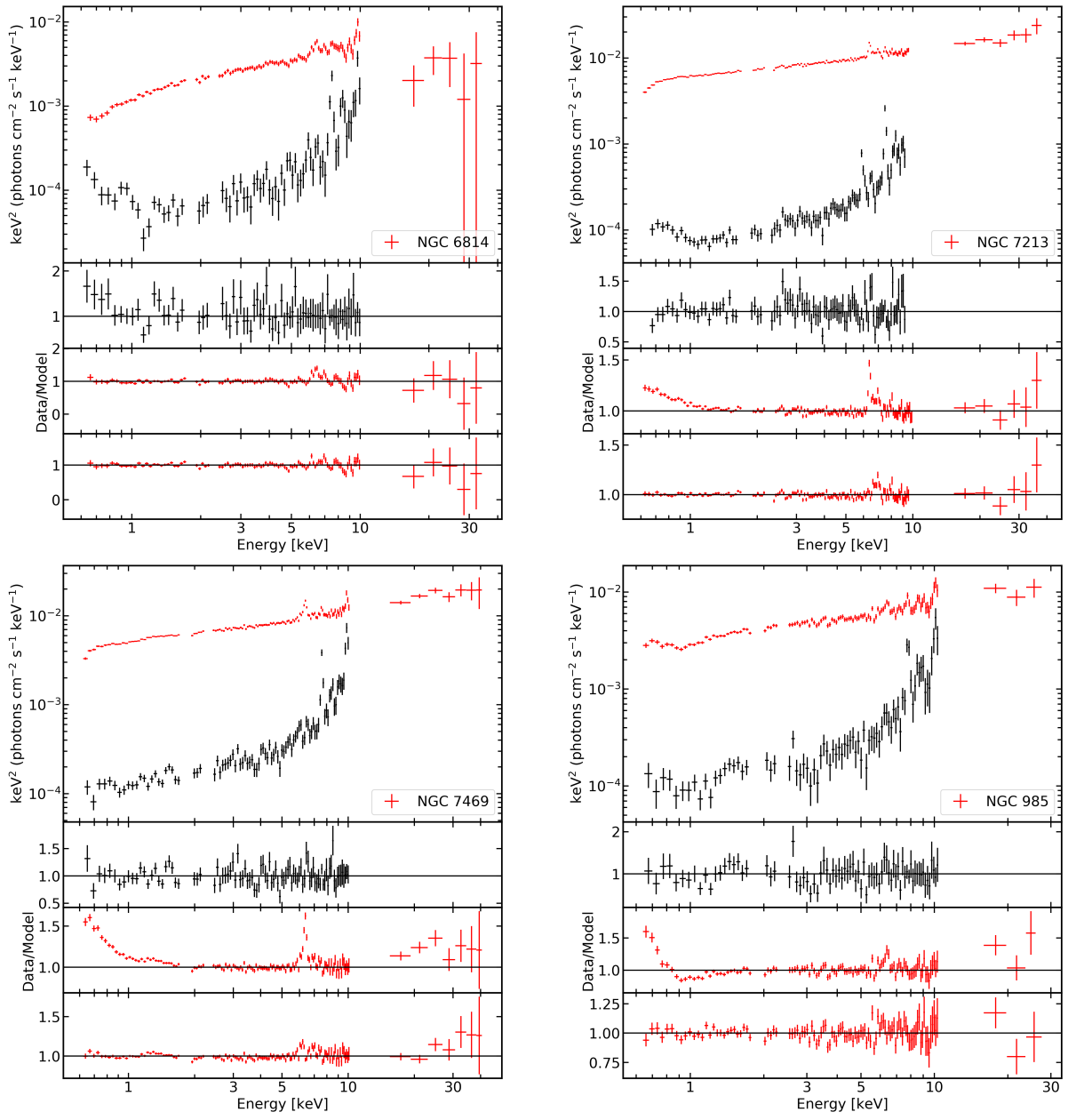


Figure A1. continued

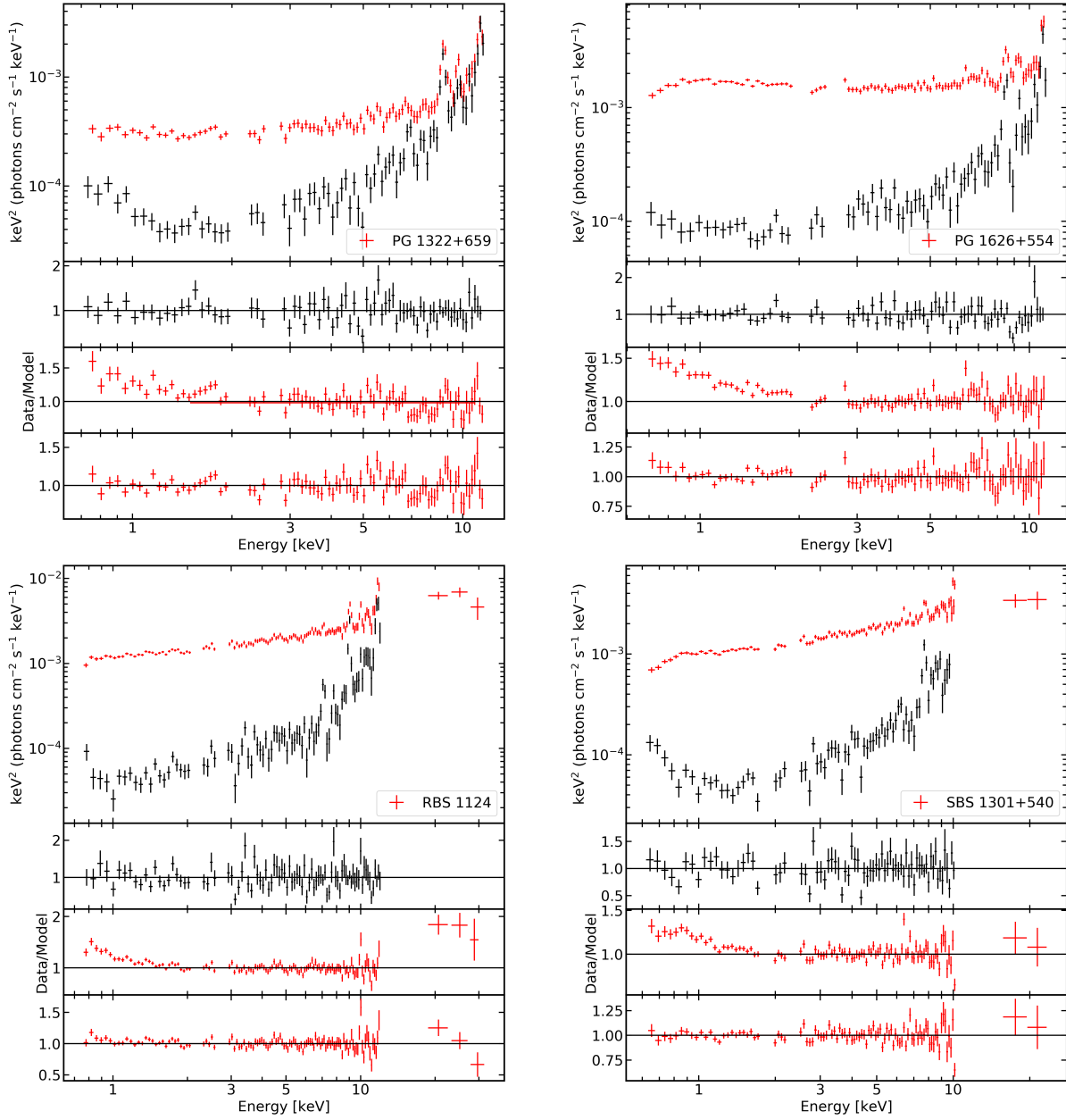


Figure A1. continued

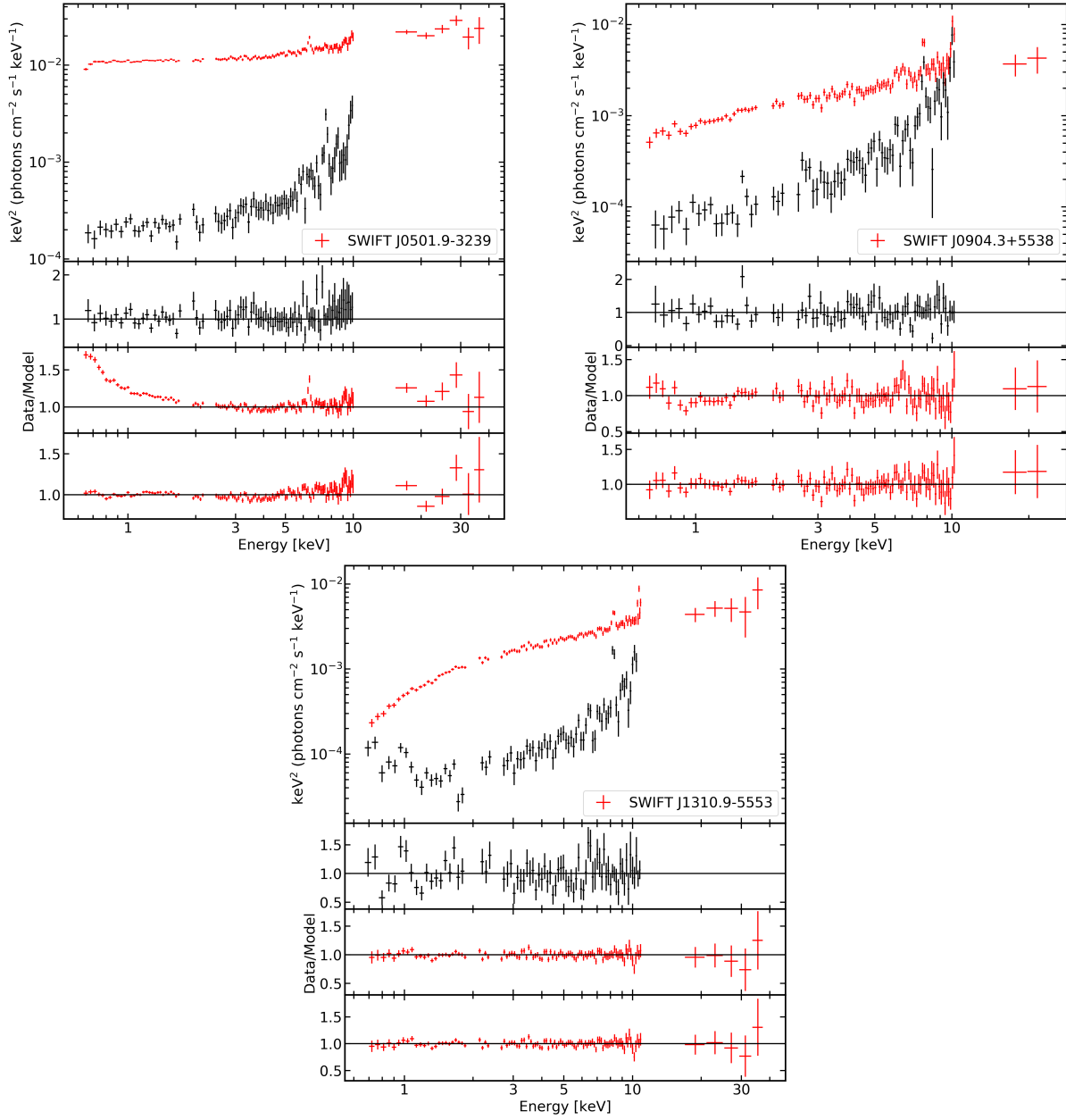


Figure A1. continued

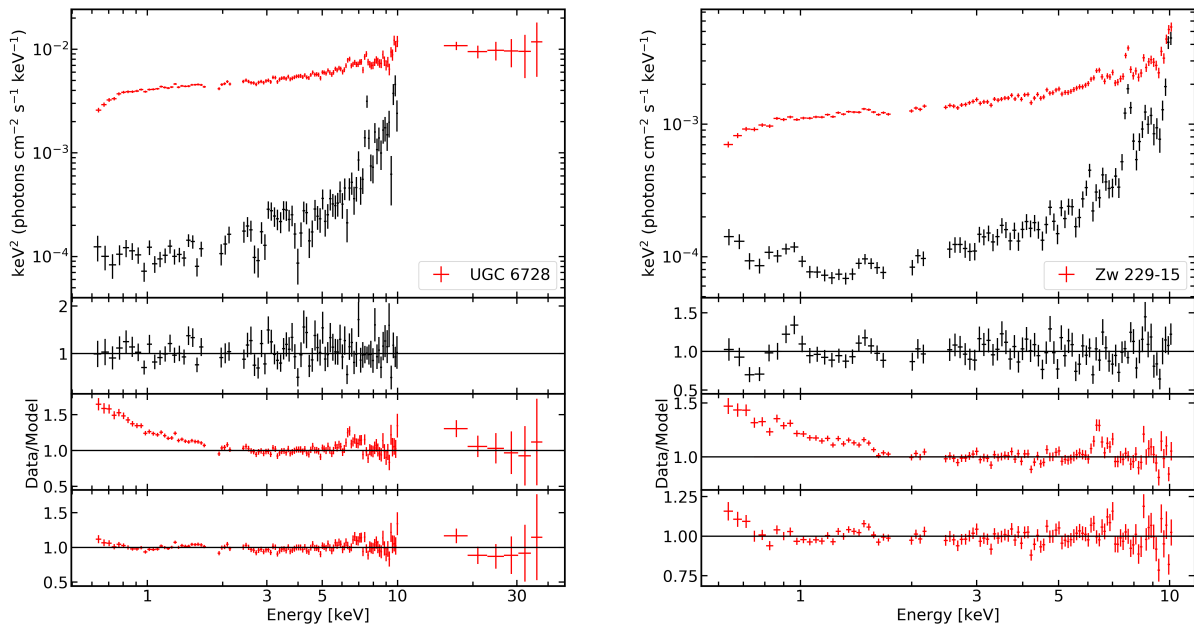


Figure A1. continued